THE ASTROPHYSICAL JOURNAL, 402:514–531, 1993 January 10

SIMULTANEOUS *ROSAT*, *GINGA*, VLA, *IUE*, AND OPTICAL OBSERVATIONS OF THE BRIGHT QUASAR H1821+643

MICHIEL KOLMAN[1] AND JULES P. HALPERN[1]
Columbia Astrophysics Laboratory, Columbia University, 538 West 120th Street, New York, NY 10027

CHRIS R. SHRADER[1,2]
Astronomy Programs, Computer Sciences Corporation, Code 668.1, NASA/GSFC, Greenbelt, MD 20771

ALEXEI V. FILIPPENKO[1,3,4]
Astronomy Department, University of California, Berkeley, CA 94720

AND

HENNER H. FINK AND STEPHAN G. SCHAEIDT
Max Planck Institut für Extraterrestrische Physik, Karl Schwarzschildstrasse 1, W-8046 Garching bei München, Germany
Received 1992 April 23; accepted 1992 July 16

ABSTRACT

We report on the first simultaneous optical, UV, and X-ray spectroscopy of the low-redshift ($z = 0.297$), high-luminosity QSO H1821+643. This multiwavelength campaign was complemented by optical imaging and radio mapping with the VLA. Although there was no significant variability during the 40 day monitoring period in either the UV or X-ray bands, a number of new results were obtained. There is significant variability in the optical, UV, and X-ray bands on time scales of years, both in flux level and spectral shape. In the co-added ultraviolet spectrum we detected a Lyman-α absorption line at $z = 0.225$. In the radio map the QSO is extended in the north-south direction at 20 cm, and can be resolved into two separate components at 6 cm. In the *ROSAT* data we separated (both spatially and spectroscopically) the emission originating in H1821+643 from the nearby hot white dwarf K1−16, and thus we isolated the intrinsic soft X-ray excess in the QSO. The *IUE* and *ROSAT* data were combined with new optical spectroscopy and hard X-ray data from *Ginga*, to reveal a strong optical/UV bump with a flat slope ($\alpha \sim -0.96, f_\nu \propto \nu^\alpha$) in the UV, a steep soft X-ray excess ($\alpha \sim -4$) between $\sim$0.15 keV and $\sim$0.5 keV, and a typical hard X-ray slope of $\alpha \sim -0.8$ extending up to 10 keV. While the optical/UV bump and the soft X-ray excess can each be fit satisfactorily with standard accretion disk models, a joint fit to the optical/UV/X-ray bump cannot be achieved. This suggests that either the optical/UV or the soft X-ray emission do not arise in an accretion disk, or that the standard bare disk model should be modified (possibly by inclusion of electron scattering) to account for both the strong, flat UV emission and the steep, soft X-ray excess.

Subject headings: quasars: individual (H1821+643) — radio continuum: galaxies — ultraviolet: galaxies — X-rays: galaxies

1. INTRODUCTION

Knowledge about emission mechanisms in QSOs can be advanced by studies across the electromagnetic spectrum. H1821+643, which distinguishes itself from other radio-quiet QSOs by its brightness ($V = 14.2$ mag), has been studied from the radio to the X-ray bands by Kolman et al. (1991, hereafter KHSF). They found that H1821+643 displayed a strong optical/UV bump and, possibly, a similarly strong, variable soft X-ray excess, although the nonsimultaneity of the observations hampered a study of the connection between the UV and soft X-ray emission.

When H1821+643 was first detected in 1977 by *HEAO A-2* (in the 0.5–20 keV range), it displayed a very strong soft X-ray excess below 2 keV (Pravdo & Marshall 1984). *Einstein* IPC observations taken 3 years later in the 0.1–3.5 keV range did not show evidence for a soft X-ray excess (KHSF), indicating that the soft X-ray flux had decreased by a factor of 4 (Pravdo & Marshall 1984). Subsequent *EXOSAT* observations in 1985 showed evidence in the combined LE-ME fits for a soft X-ray excess, but with a flux a factor of $\sim$10 below the soft component from the *HEAO A-2* observations (Warwick, Barstow, & Yaqoob 1989). The poor energy resolution of the low energy (LE) telescope on *EXOSAT* did not allow for further study of the soft X-ray excess.

As the field of view of the *HEAO A-2* low energy detector (LED) is quite large, it is possible that the detected soft X-ray emission was in part due to nearby stars, such as SAO 17828 and SAO 17878, in addition to K1−16, a planetary nebula only 90″ from the QSO (KHSF). KHSF estimated the contribution from the SAO stars to the LED flux based on the IPC observations, and concluded that these stars could not have accounted for the strong LED flux, although considering the poor energy resolution of the IPC below $\sim$1 keV, it could not be ruled out that K1−16 contaminated the *HEAO A-2* LED detection.

The *ROSAT* observations presented here, obtained with the position-sensitive proportional counter (PSPC) over a period of 40 days, provide the best X-ray spectra of H1821+643 in the 0.1–2.4 keV range. The PSPC is therefore the ideal instrument to study the soft X-ray excess in H1821+643 and to address

[1] Guest Observer, International Ultraviolet Explorer Satellite.
[2] Staff member, GRO Science Support Center, NASA/GSFC.
[3] Guest Observer, Palomar Observatory, which is owned and operated by the California Institute of Technology.
[4] Presidential Young Investigator.

the issue of possible contamination of the *HEAO A-2* spectrum by nearby sources such as K1 – 16.

While there are alternative models such as that of Barvainis (1990), who suggested that the optical/UV emission is optically thin free-free radiation, the optical/UV bump is generally attributed to an accretion disk around the central black hole (e.g., Malkan & Sargent 1982). In this picture the soft X-ray excess can be interpreted as the high-energy tail of the XUV bump. If both the soft X-ray and UV emissions arise in an accretion disk, then this should be reflected in the continuum energy distribution and the correlated variability of the UV and X-ray flux. However, this interpretation has not been well tested in the past due to the lack of simultaneous coverage in the UV and soft X-ray bands and the poor sensitivity to soft X-rays. The simultaneous observations of H1821+643 with *IUE* and *ROSAT* provide the first test of the common origin of the UV bump and soft X-ray excess in any QSO. Due to its location in the sky, which allowed for extensive coverage during the *ROSAT* All Sky Survey, and its strong and variable emission detected in the UV and at soft X-ray energies, H1821+643 has become the prime object for such a study. Although the main thrust of this paper is observational, we will also briefly discuss the interpretation of the continuum energy distribution in the framework of accretion disk models.

2. OBSERVATIONS

2.1. *X-Ray Observations*

X-ray observations of H1821+643 in 0.07–2.4 keV band were obtained by the *ROSAT* PSPC during the All Sky Survey (RASS). During the survey the ecliptic poles received full coverage and objects close to the poles were observed for long periods. H1821+643, located only 3° from the north ecliptic pole, was in the field of view of *ROSAT* from 1990 October 14 to 1990 November 24. The details of these observations are given in Table 1. The PSPC image centered on H1821+643 is shown in Figure 1. In the northeast corner, the previously known X-ray source SAO 17878 is visible. The photons from the QSO are extracted within a 6′ radius around the centroid of H1821+643, while the background is obtained from an annulus with an inner and outer radius of 11′ and 30′, respectively. About 35′ south of H1821+643 there is evidence for several weak sources, which are excluded in the calculation of the background counts, as well as a weak unidentified X-ray source 15′ east of the QSO. H1821+643 is a strong source, with an observed count rate (uncorrected for vignetting and the obscuring rib structure) of 0.83 counts s^{-1}, about 10 times the local background rate.

TABLE 1

ROSAT PSPC OBSERVATIONS OF H1821+643

Parameter	Value
Observation period (Julian day −2448000)	178.9–219.6
Total exposure time(s)	9049
Source counts:	
Total counts (within 6′ from QSO)	7525
Count rate (counts s^{-1})	0.83
Background counts:	
Total counts (in 11′–30′ annulus)	15727
Surface brightness (counts s^{-1} $arcmin^{-2}$)	7.7×10^{-4}
Counts within 6′ from QSO	788
F_X(0.1–2.4 keV)[a]	1.56×10^{-11}
L_X(0.1–2.4 keV)[b]	2.82×10^{46}

[a] Flux (ergs cm^{-2} s^{-1}) in observed energy band, using the spectral model described in § 3.3.

[b] Luminosity (ergs s^{-1}) in intrinsic energy band, corrected for absorption and assuming the spectral model described in § 3.3, $H_0 = 50$ km s^{-1} Mpc^{-1}, and $q_0 = 0$.

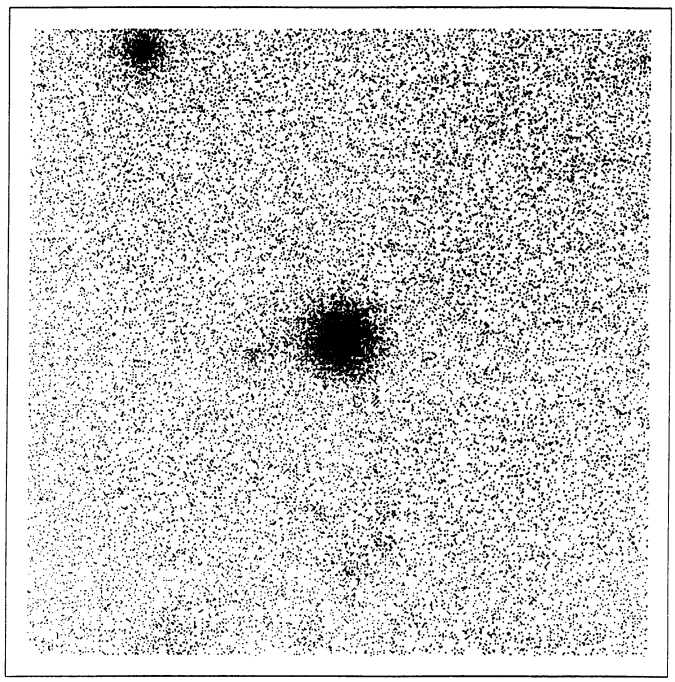

FIG. 1.—X-ray image around H1821+643 obtained with the PSPC in the 0.09–2.4 keV range during the *ROSAT* All Sky Survey. North is up and east is left. SAO 17878 is visible in the northeast corner. Weak X-ray sources can be seen 35′ south and 15′ east of H1821+643.

During the period that H1821+643 was in the field of view of *ROSAT*, *Ginga* obtained X-ray spectra on two occasions (1990 October 24 and 28). The flux in the 2–10 keV interval was 2.09×10^{-11} and 1.95×10^{-11} ergs s^{-1} cm^{-2}, respectively, while the corresponding power-law photon index was 1.78 and 1.83 (F. Makino 1991, private communication).

2.2. *Ultraviolet Observations*

The details of the new *IUE* observations, which we obtained simultaneously with the *ROSAT* survey (under the RIASS program), are listed in Table 2. The images were obtained with the large aperture in the low-dispersion mode, resulting in a spectral resolution of ∼5 and ∼8 Å for the SWP and LWP, respectively. The spectra were obtained from the line-by-line images with the Gaussian extraction routines at the Goddard Regional Data Analysis Facility to minimize the noise while maintaining accurate flux levels. Both the SWP and LWP data are corrected for the slight temperature dependence of the detector sensitivity. The LWP data were calibrated with the accurately determined standards obtained in 1984–1985 (Cassatella, Lloyd, & Riestra 1988). The more uncertain 1980 May flux calibration was used for the SWP data. The accuracy of this calibration is estimated at ∼10% (Bohlin & Holm 1980), but work by Finley, Basri, & Bowyer (1990) suggests

TABLE 2

NEW *IUE* OBSERVATIONS OF H1821+643

Image	Integration time (minute)	Date
SWP 39826.....	290	1990 Oct 13
LWP 19005.....	123	1990 Oct 13
SWP 39868.....	270	1990 Oct 19
LWP 19035.....	108	1990 Oct 19
SWP 39930.....	290	1990 Oct 23
LWP 19054.....	120	1990 Oct 23
SWP 39985.....	279	1990 Oct 28
LWP 19085.....	120	1990 Oct 28
SWP 40046.....	280	1990 Nov 4
LWP 19144.....	106	1990 Nov 4
SWP 40089.....	272	1990 Nov 9
LWP 19182.....	100	1990 Nov 9
SWP 40103.....	271	1990 Nov 13
LWP 19219.....	100	1990 Nov 13

that the actual calibration could be 10%–15% different from the 1980 May calibration.

We corrected the spectra for the effects of interstellar reddening, using the extinction curve of Seaton (1979) and $E(B-V) = 0.085$ mag. The color excess is based on the $N_H/E(B-V)$ ratio of 4.8×10^{21} cm^{-2} mag^{-1} (Bohlin, Savage, & Drake 1978) and the neutral hydrogen column density in the direction of H1821+643 ($N_H = 4.1 \times 10^{20}$ cm^{-2}, Stark et al. 1992; Heiles 1975 gives a slightly larger but more uncertain value of 5×10^{20} cm^{-2}). We did not correct for any internal reddening, as the intrinsic extinction in QSOs is thought to be very small (Sun & Malkan 1989, and references therein). Seven SWP and seven LWP spectra were coaded with the resulting spectrum shown in Figure 2. Despite the decline in sensitivity below 1200 Å, there is strong emission shortward of the Lyman limit (which is redshifted to 1182 Å), as reported earlier in KHSF.

2.3. *Radio Observations*

We observed H1821+643 in the 20 cm continuum band with the NRAO[5] VLA in the A-array on 1991 September 10. The exposure time was 21 minutes. In the calibrated and CLEANed map (Fig. 3*a*), we detected H1821+643 at its optical position as well as a double-peaked radio source ~50″ to the north. The flux of H1821+643 at 20 cm is 31.4 mJy (Table 3). Neff & Hutchings (1992) reported an upper limit at 6 cm, but this was obtained at the inaccurate position quoted in Pravdo & Marshall (1984; the precise position is given in KHSF). The flux at 6 cm (obtained in A-array almost a year before the monitoring campaign) is actually 10.8 mJy (S. Neff 1992, private communication; Table 3). The radio image of H1821+643 at 20 cm is extended on a length scale of $\lesssim$15″ in the north-south direction. In the higher spatial resolution map at 6 cm (Fig. 3*b*), two separate components about 2″ apart are distinguished in the QSO. The northern component has a total flux of 9.2 mJy and the southern component only 1.4 mJy. The optical position is close (0.″8) to the northern component. Given the ~1″ uncertainty in the optical position, it is probably coincident with the northern component.

[5] The National Radio Astronomy Observatory is operated by Associated Universities, Inc., under cooperative agreement with the National Science Foundation.

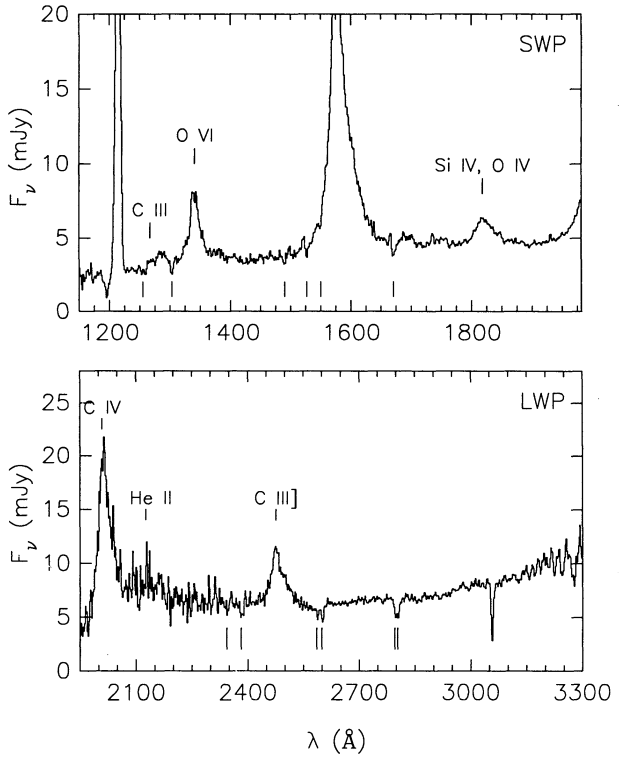

FIG. 2.—Co-added spectrum of H1821+643 obtained with *IUE* in 1990, corrected for the estimated interstellar extinction of $E(B-V) = 0.085$ mag. The Lyman-α emission (peaking around 1580 Å) is saturated. Strong reseaux are present around 1190 Å and 3050 Å. The emission line around 1216 Å is geocoronal Lyman-α. The vertical tick marks indicate the detected absorption lines (Table 11). Note the strong flux below the Lyman limit at 1182 Å.

2.4. *Optical Imaging*

Optical CCD imaging was obtained by J. Hibbard on 1991 August 30 with the 2.1 m telescope at Kitt Peak National Observatory. The ST1K CCD chip was used with the Harris-*R* filter. The observational conditions were not photometric. Figure 4 is the sum of two 300 s exposures. Hutchings & Neff (1991, hereafter HN) obtained deep CCD images in several bands under photometric conditions, from which they concluded that H1821+643 is an unusually red QSO. We show in § 7 that this QSO is more likely blue than red.

TABLE 3

VLA OBSERVATIONS OF H1821+643

Object	R.A. (1950)	Decl. (1950)	Peak Flux (20 cm) (mJy beam^{-1})	Total Flux (20 cm) (mJy)	Total Flux[a] (6 cm) (mJy)
QSO	$18^h21^m41^s.79$	64°19′ 1.″0	14.8	31.4 ± 0.6	10.6
Galaxy "A"	18 21 39.60	64 19 42.0	7.5	42.2 ± 1.0	5.7

[a] 6 cm observations from S. Neff (1992, private communication).

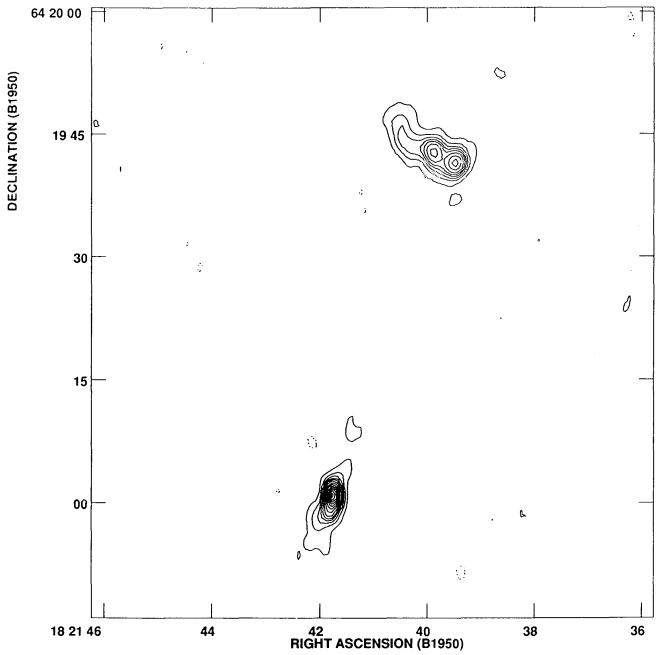

FIG. 3a

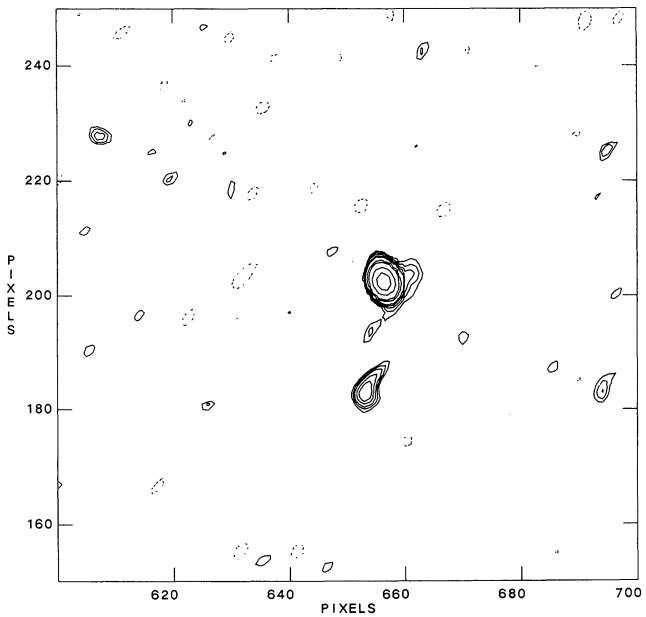

FIG. 3b

FIG. 3.—(*a*) Radio map in the 20 cm band. H1821+643 is the southern source. Note the extended structure of H1821+643 on a scale of $\lesssim 15''$ in the north-south direction. (*b*) Radio map of H1821+643 in the 6 cm band (from S. Neff). The scale is 0".1 per pixel (which is shown on the axes). Note that H1821+643 is resolved into two components about 2″ apart. The optical position is coincident with the brightest, northern component.

In addition to H1821+643, the optical counterpart of the northern double radio source (see Fig. 3) is also visible in Figure 4. It is galaxy "A" of Schneider et al. (1992), an elliptical in the same cluster as the QSO. Schneider et al. also found a foreground galaxy 32″ from the QSO at a redshift of 0.226 (galaxy "G"). With $H_0 = 50$ km s^{-1} Mpc^{-1} and $q_0 = 0$ (which are used throughout this paper), this corresponds to a projected separation of 173 kpc. In § 6, we discuss a Lyman-α absorption line which is detected in the ultraviolet spectrum of the QSO at this redshift.

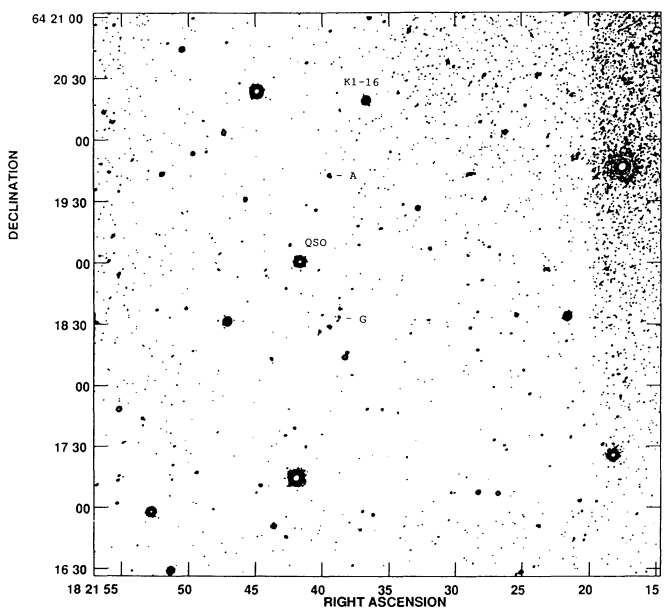

FIG. 4.—Optical *R*-band image around H1821+643 (indicated by "QSO"). Also visible is galaxy "A" of Schneider et al. (1992) which is coincident with the northern radio source (Fig. 3*a*), and the nearby white dwarf K1−16. The foreground galaxy "G" ($z = 0.226$) of Schneider et al. is also labeled.

2.5. *Optical Spectroscopy*

Moderate-resolution optical spectroscopy was obtained on 1990 November 28 with the Double Spectrograph on the Palomar 5.0 m reflector, through an 8″ slit during several 500 s exposures under photometric conditions. The wavelength range was 3446–9922 Å. This spectrum is shown in Figure 5. Additional optical spectra were obtained at Lick Observatory before and during the *IUE-ROSAT* monitoring campaign (Table 4) with a larger wavelength range but lower resolution. These data were obtained with the UV Schmidt spectrograph (Miller & Stone 1987) at the Cassegrain focused of the 3.0 m Shane reflector. A wide slit (6″–10″, depending on the seeing and on the amount of moonlight) was used to obtain an accurate measurement of the flux. Standard stars were observed with the same slit width. The data were flattened with exposures of the dome, illuminated by a featureless quartz lamp. Comparison lamps (He-Hg-Cd-Ne-Ar) were used to establish the wavelength scale. Atmospheric absorption bands were removed through division by spectra of standards stars which are intrinsically featureless at the appropriate wavelengths. The spectrum obtained at Lick Observatory on 1990 October 20 with a wavelength range of 3100–9870 Å was used to study the continuum energy distribution (§ 8). The optical and ultraviolet spectra match up very well in the near-UV.

3. X-RAY SPECTRAL ANALYSIS

3.1. *Power-Law Fit*

We first attempted a fit with a power-law model to the coadded X-ray spectrum. Even if this simple model does not

TABLE 4

OPTICAL SPECTRA OF H1821+643[a]

Date	Wavelength Range (Å)	Resolution (Å)	Comments
88 Jul 01	6000–7600	3–8	
88 Jul 17	6000–7600	6–8	
88 Jul 18	6000–7600	6–8	
88 Sep 15	6000–7000	6–8	
88 Sep 18	3100–10000	13–16	bad seeing
88 Oct 3	3100–10000	12–14	
89 Apr 28	3138–10046	12–14	
89 Jul 9	3100–8900	12–14	
89 Jul 10	3900–7100	12–14	
90 Mar 25	3900–7100	12–14	
90 Apr 1	3900–7100	12–14	
90 May 1	3400–9800	6–14	
90 Jul 30	3106–9850	6–14	
90 Aug 30	3100–9900	6–14	
90 Sep 27	3900–9900	12–14	photometric?
90 Oct 20	3108–9852	6–14	
90 Nov 11	3100–9870	6–14	photometric?
90 Nov 28	3446–9922	6–9	Palomar 5.0 m
91 Jul 20	3100–9900	12–14	Clouds
91 Aug 4	3100–9900	6–14	

[a] All spectra obtained at Lick Observatory with the 3.0 m Shane reflector, with the exception of 1990 November 28. All spectra were obtained under photometric conditions unless indicated otherwise.

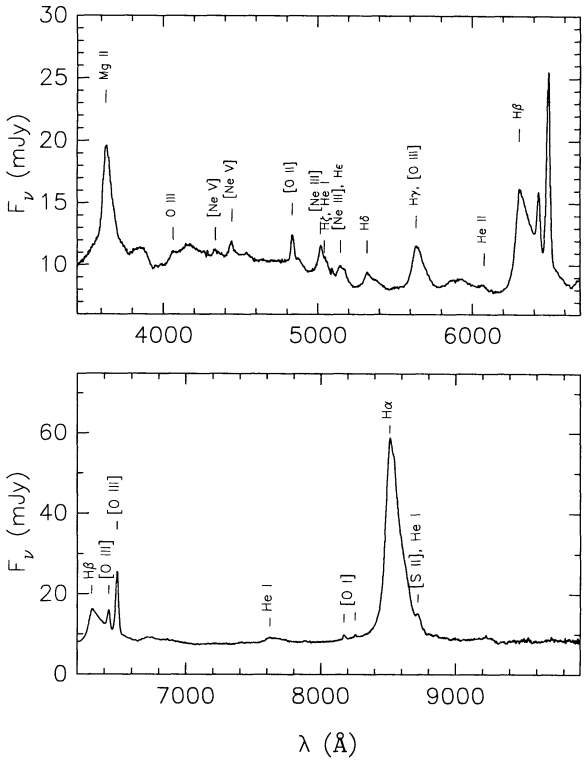

FIG. 5.—Optical spectrum obtained with the Palomar 5.0 m reflector on 1990 November 28 under photometric conditions. The interstellar extinction correction for $E(B-V) = 0.085$ mag has been applied. The continuum appears bumpy due to the contribution of the blended Fe II lines (e.g., around 3850, 4200, 5900, and 6700 Å).

adequately fit the data, the deviations provide clues to the nature of the physical phenomena which shape the spectrum, thus guiding more detailed modeling. In addition to the usual photon index α, we parameterize the standard interstellar medium absorption cross section $\sigma(E)$ of Morrison & McCammon (1983) by the equivalent neutral hydrogen column density N_H. The spectrum is thus

$$F_1(E) = F_{pl}(E, \alpha)e^{-\sigma(E)N_H}, \quad (1)$$

where F_{pl} is given by

$$F_{pl}(E) = A_{pl}(E/E_0)^{-\alpha}, \quad (2)$$

with A_{pl} as the spectral flux at the reference energy E_0 (= 1 keV). The results of the fit are given in Table 5. Significant deviation from the power law is apparent in Figure 6 at the low-energy end ($E \lesssim 0.2$ keV), thus suggesting the presence of a soft component. The fit value for N_H of $(1.22 \pm 0.22) \times 10^{20}$ cm^{-2} is significantly smaller than the hydrogen column density inferred from the 21 cm observations, i.e., 4.1×10^{20} cm^{-2} (Stark et al. 1992).

3.2. *Power-Law plus Soft X-Ray Excess*

As AGNs frequently display a soft X-ray excess (Wilkes et al. 1989; Turner & Pounds 1989; Comastri et al. 1992; Masnou et al. 1992) and the power-law fit displays strong deviations in the softest X-ray channels, we fit the spectrum with a power-law plus a soft X-ray component, which we modeled in three different ways. Since this requires more free parameters than can be justified considering the spectral resolution of the PSPC, we fixed parameters such as N_H (at the Galactic value) and α (at

TABLE 5

ROSAT TWO-COMPONENT FITS[a]

Fit	α	N_H (10^{20} cm^{-2})	A_{pl}[b]	A_{bb}[b]	kT_{bb} (eV)	A_{th}[b]	kT_{th} (eV)	α_b	χ^2/d.o.f.
pl[c]	1.55 ± 0.09	1.22 ± 0.22	4.61 ± 0.15						90/64 = 1.40
pl, bb[c]	1.55*	4.1*	5.04 ± 0.15	3.77 ± 4.21	16.8 ± 0.2				122/64 = 1.91
pl, bb[c]	1.75*	4.1*	5.04 ± 0.19	1.62 ± 2.22	24.4 ± 0.5				126/64 = 1.97
pl, bs[d]	1.75*	4.1*	4.99 ± 0.12			9.11 ± 0.44	75*		158/65 = 2.43
bpl[d]	1.75*	4.1*	1.33 ± 2.43[e]					9.83 ± 0.11	90/64 = 1.40
bpl[d]	1.90*	4.1*	4.92 ± 1.27[e]					8.97 ± 0.19	85/64 = 1.31

[a] An asterisk (*) denotes a fixed parameter.

[b] Normalization at 1 keV after a posteriori correction for deadtime and the supporting structure of the PSPC entrance window. A_{pl} is in 10^{-3} photons cm^{-2} s^{-1} keV^{-1}, A_{bb} is in photons cm^{-2} s^{-1}, and A_{th} is in 10^{-7} photons cm^{-2} s^{-1} keV^{-1}.

[c] pl: power-law, bb: black body. Errors are 68% confidence for three interesting parameters.

[d] bs: bremsstrahlung, bpl: broken power-law. Errors are 68% confidence for two interesting parameters.

[e] In 10^{-7} photons cm^{-2} s^{-1} keV^{-1}.

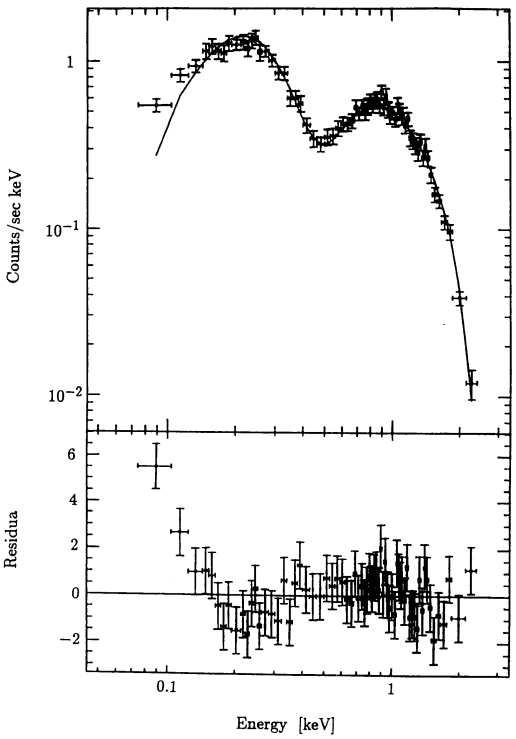

FIG. 6.—X-ray spectrum obtained with the *ROSAT* PSPC, fitted with a simple power-law model (Table 5). Note the strong deviations at low energies ($E < 0.2$ keV).

those values which resulted in a minimum χ^2 in the simple power-law fit).

1. *Power-law plus blackbody fit.*—We modeled the soft X-ray component by a blackbody fit. This model has two more parameters than the simple power-law fit, namely the blackbody temperature T_{bb} and the normalization A_{bb}. The model spectrum is thus

$$F_2(E) = [F_{pl}(E, \alpha) + F_{bb}(E, kT_{bb})]e^{-\sigma(E)N_H}, \quad (3)$$

where F_{pl} is defined in equation (2) and

$$F_{bb}(E) = A_{bb}\frac{1}{2.404kT_{bb}}\frac{(E/kT_{bb})^2}{e^{E/kT_{bb}} - 1}. \quad (4)$$

We fixed N_H at 4.1×10^{20} cm^{-2}, E_0 at 1 keV, and α at 1.55 or 1.75 (where the latter value is consistent with the power-law slope as measured by *Ginga*), leaving A_{pl}, A_{bb}, and kT_{bb} as free parameters. The results of the fit are presented in Table 5 and shown in Figure 7. The residuals still deviate strongly at the low energy channels, which is true for either value of α.

2. *Power-law plus bremsstrahlung fit.*—In an attempt to model the soft X-ray excess more successfully we fitted a power-law plus a thermal bremsstrahlung model. Again, N_H is fixed at its Galactic value, α at 1.75, E_0 at 1.0 keV, and the bremsstrahlung energy at $kT_{th} = 75$ eV (as optimized in previous fits which are not shown here), leaving two free parameters, namely A_{pl} and A_{th}. The fitting model is thus given by

$$F_3(E) = [F_{pl}(E, \alpha) + F_{th}(E, kT_{th})]e^{-\sigma(E)N_H}, \quad (5)$$

where

$$F_{th}(E) = A_{th}(E/E_0)e^{-(E-E_0)/kT_{th}}g(E, kT_{th})/g(E_0, kT_{th}); \quad (6)$$

g is the Gaunt factor. Results are given in Table 5. The reduced χ^2 is quite high (2.43), indicative of a bad fit. The residuals are very similar to Figure 7, i.e., strongly deviating at low energies.

3. *Broken power-law fit.*—Finally, we fitted the spectrum with a broken power-law fit. The model is given by

$$F_4(E) = \begin{cases} A_{pl}(E/E_0)^{-\alpha_b}e^{-\sigma(E)N_H} & E < E_b \\ A_{pl}(E_b/E_0)^{\alpha-\alpha_b}(E/E_0)^{-\alpha}e^{-\sigma(E)N_H} & E \geq E_b \end{cases}. \quad (7)$$

Here we fixed α at 1.75 or 1.90, and N_H at 4.1×10^{20} cm^{-2}. The quantity E_0 is 1 keV and E_b equals 0.27 keV. Two free parameters remain, namely A_{pl} and α_b. Results are given in Table 5. Even with a high value of ~ 10 for α_b, the spectrum could not be fitted adequately at low energies and again the residuals are very similar to those in Figure 7.

In summary, the observed spectrum cannot be fitted statisfactorily with a two-component model, i.e., a power-law and a soft X-ray excess. In every attempt significant deviations between the spectral model and the data remain in the lower energy channels.

3.3. *Three-Component Fits*

Since we could not model the spectrum successfully with a two-component model, we introduced an additional component to account for the excess at the very low energy channels. This model consists of a power-law, a soft X-ray excess, and an ultrasoft component. As such a three-component fit requires more parameters than can be justified by the spectral resolution of the PSPC, the fits were performed iteratively where only two parameters were allowed to vary during each step. After these free parameters were optimized, they were fixed in the next fitting round in which two other parameters were treated as free parameters. The adopted ultrasoft com-

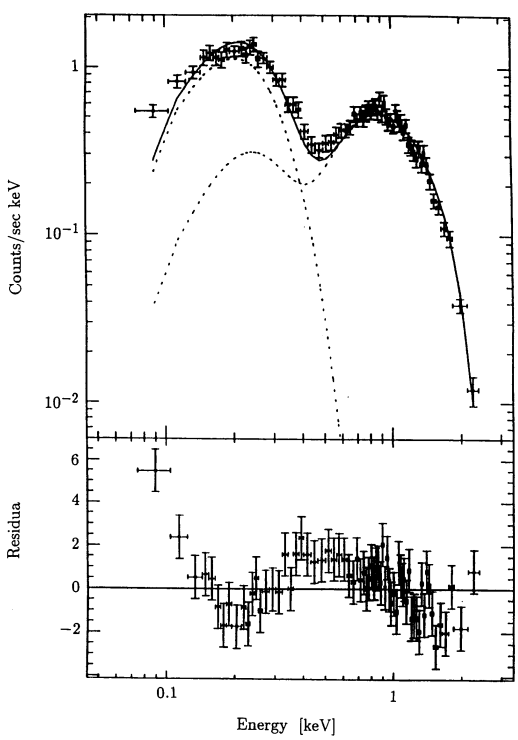

FIG. 7.—X-ray spectrum obtained with the *ROSAT* PSPC, fitted with a power-law plus blackbody model (Table 5). Note the strong deviations at low energies ($E < 0.2$ keV).

TABLE 6

ROSAT ULTRASOFT FITS[a]

Fit	α	N_H (10^{20} cm^{-2})	A_{pl}[b]	A_{bb}[b]	kT_{bb} (eV)	A_{th}[b]	kT_{th} (eV)	α_2	A_{pl_2}[b]	χ^2/d.o.f.[c]
pl, bb[d]	1.82 ± 0.11	4.1*	5.04 ± 0.28	0.11 ± 0.25	40.0 ± 28.4					39/66 = 0.60
bb[e]		0.0 ± 4.7		0.57 ± 5.56	11.6 ± 41.4					
pl, bs[d]	1.81 ± 0.05	4.1*	5.03 ± 0.12			4.8 ± 30.9	73.1 ± 27.8			38/66 = 0.58
bb[e]		0.0*		0.57*	11.6*					
pl, pl[d]	1.81 ± 0.05	4.1*	4.94 ± 0.12					5.13 ± 0.96	7.17 ± 4.30	40/66 = 0.60
bb[e]		0.0*		0.57*	11.6*					
pl[f]	1.79 ± 0.10	2.22 ± 0.30	4.81 ± 0.16							44/65 = 0.67
bb[e]		0.0*		0.57*	11.6*					
pl[f]	1.73 ± 0.03	1.90 ± 0.28	4.75 ± 0.11							37/65 = 0.56
bb[e]		0.0 ± 6.1		98 ± 2259	6.57 ± 1.90					

[a] An asterisk denotes a fixed parameter.

[b] Normalization at 1 keV after a posteriori correction for occulting rib structure and deadtime. A_{pl} is in 10^{-3} photons cm^{-2} s^{-1} keV^{-1}, A_{bb} is in photons cm^{-2} s^{-1}, A_{th} is in 10^{-7} photons cm^{-2} s^{-1} keV^{-1}, and A_{pl_2} is in 10^{-5} photons cm^{-2} s^{-1} keV^{-1}.

[c] Reduced χ^2 for the combined fit of the ultrasoft component and the power-law plus soft X-ray excess components.

[d] Parameters were stepwise successively optimized by choosing two parameters free in each fitting step. Errors are 68% confidence for two interesting parameters; pl: power-law, bb: blackbody, bs: bremsstrahlung.

[e] Blackbody fit to ultrasoft component ($E \lesssim 0.15$ keV).

[f] Errors are 68% confidence for three interesting parameters.

ponent is a blackbody with a temperature T_1 and a hydrogen column density N_1. The soft X-ray excess has either temperature T_2 or photon index α_2, and hydrogen column density N_2, fixed at the Galactic value. The model is thus given by

$$F_5(E) = F_{bb}(E, kT_1)e^{-\sigma(E)N_1} + [F_{pl}(E, \alpha) + F_{se}]e^{-\sigma(E)N_2}, \quad (8)$$

where F_{pl} is defined in equation (2), F_{bb} in equation (4), F_{th} in equation (6), and where F_{se} describes the soft excess [$F_{se} = F_{bb}(E, kT_2)$, $F_{th}(E, kT_2)$, or $F_{pl}(E, \alpha_2)$]. We modeled this soft excess in three different ways.

1. *Soft excess fit by a blackbody model.*—We fitted the soft excess component with a blackbody model, defined in equation (4). Therefore, two blackbody components are used here: one to describe the ultrasoft component and a second to describe the soft X-ray excess. The results are given in Table 6. The parameters of the fit to the ultrasoft component are not well constrained as no turnover is detected within the energy range of *ROSAT*. This fit indicates a temperature of log $T_1 = 5.13$. While the contribution from the power-law and soft excess components decline below $\sim$0.25 keV, the ultrasoft component continues to rise down to the lowest energy channel, dominating the emission below $\sim$0.17 keV. The reduced χ^2 of 0.60 shows that this is a satisfactory fit. The column density of the ultrasoft component had a best fit value of $(0.0 \pm 4.7) \times 10^{20}$ cm^{-2}, which we fixed at 0.0 in subsequent fits. This small value of N_1 suggests that the ultrasoft component originates within our galaxy.

2. *Soft excess fit by a bremsstrahlung model.*—We fitted thermal bremsstrahlung, defined in equation (6), as the soft excess model. The parameters of the ultrasoft component were fixed at the values obtained in the previous fit. Results are listed in Table 6. Again the low χ^2_{red} (0.58) indicates a good fit. The error on the normalization of the bremsstrahlung component (A_{th}) is large, indicating that the strength of the soft X-ray excess is not well determined.

3. *Soft excess fit by a power-law model.*—We used a power-law model to describe the soft X-ray excess. Again the fit parameters of the blackbody component and the column density are fixed. We were able to obtain a satisfactory fit ($\chi^2_{red} = 0.60$) with the parameters listed in Table 6. The soft X-ray excess is well described by a power-law component with $\alpha_2 = 5.13 \pm 0.96$. This fit is shown in Figure 8.

We investigated whether the ultrasoft component is a separate spatial component by constructing the image in the soft band (0.09–0.40 keV; Fig. 9). Surprisingly, this image shows significant extended emission north of the QSO. As it has been suggested (Warwick et al. 1989; KHSF) that the central star of the planetary nebula K1−16 (DS Dra) could contribute to the soft X-ray band, and as this star is located 1.'3 north and 0.'5 west of H1821+643, we identify it with the ultrasoft spectral component. We extracted the photons originating from the extended emission and found a count rate of 0.091 counts s^{-1} (after background subtraction) in the 0.07–0.17 keV band, in good agreement with the spectral fit of the ultrasoft component, which gives 0.087 counts s^{-1} in this energy band. The low column density of this component is consistent with its Galactic origin. The blackbody fit and the best-fit temperature of log $T_1 = 5.13$ are also consistent with the emission from the white dwarf K1−16, as Grauer et al. (1987) estimated its temperature at log $T = 5.1$. K1−16 has also been detected in the XUV band with the Wide Field Camera on-board *ROSAT* (M. Barstow 1991, private communication).

With the ultrasoft component accounted for by K1−16, we still need to test whether a soft excess is required in the spectrum of the QSO. With the blackbody parameters of K1−16 held constant, we fitted a simple power-law to the spectrum. The N_H of the QSO was treated as a free parameter. Good fits were obtained (Table 6) with $\chi^2_{red} \approx 0.6$ but only for a column density of $(2.22 \pm 0.30) \times 10^{20}$ cm^{-2}, far below the Galactic value of 4.1×10^{20} cm^{-2}, thus indicative of a significant soft X-ray excess in the spectrum of the QSO.

Finally, to investigate whether the emission from the white dwarf could account for the soft X-ray excess attributed to the QSO, we fitted a model where both the blackbody parameters, which describe the emission from K1−16, and the power-law parameters which describe the QSO, were allowed to vary freely. Results are listed in Table 6. Again acceptable fits could be obtained only for low values of N_H for the QSO, namely $(1.90 \pm 0.18) \times 10^{20}$ cm^{-2}. Therefore, we conclude that a sig-

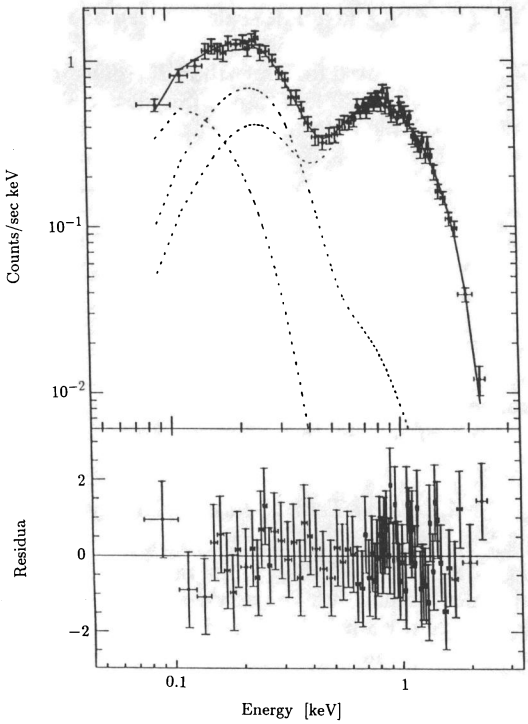

FIG. 8a

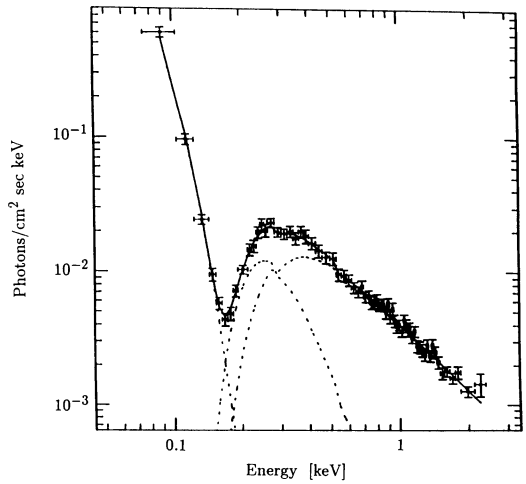

FIG. 8b

FIG. 8.—X-ray spectrum obtained with the *ROSAT* PSPC, fitted with a blackbody component to describe the low-energy channels ($E < 0.2$ keV) and two power-laws to fit the higher energies (Table 6). (*a*) Observed spectrum. (*b*) Inferred incident spectrum.

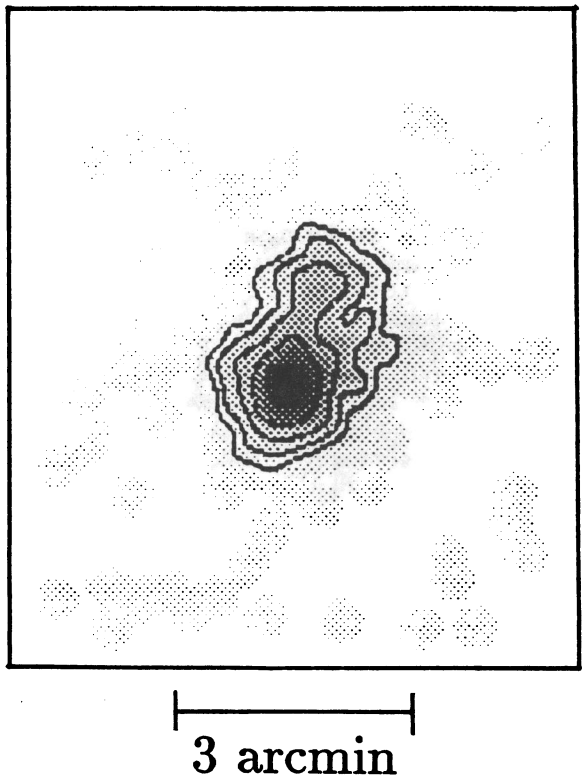

FIG. 9.—X-ray image in the soft band (0.09–0.40 keV) from the *ROSAT* PSPC. Note the extended structure to the north. This emission is identified with the white dwarf K1 – 16. North is up and east is to the left.

nificant soft X-ray excess is present in the spectrum of H1821+643. However, we cannot determine whether this soft excess is better described by a blackbody fit, bremsstrahlung fit, or a power-law fit, as all three models have equally good statistics ($\chi^2_{red} \approx 0.6$ and residuals smaller than 2 σ). We will adopt the power-law model (shown in Fig. 8) as our working model in the remainder of the paper. The parameters of the soft excess fits have large uncertainties and the strength and spectral shape of the soft excess are therefore not well determined. In conclusion, the spectrum as detected with the PSPC can only be described accurately by three components: an ultrasoft component, fitted by a blackbody curve and attributed to the white dwarf K1 – 16, and a power-law plus soft excess originating from the QSO H1821+643.

4. VARIABILITY

4.1. *Short-Term X-Ray Variability*

In order to study the variability in the X-ray band, we constructed light curves from the *ROSAT* observations during the RASS (observations are summarized in Table 1). In Figure 10 the total count rate ($E = 0.1$–2.4 keV) after correction for vignetting, scattering (especially important for the hard photons), and the obscuring rib structure of the PSPC, is shown as a function of time. The average count rate is 1.13 counts s^{-1}. Also shown are the light curves of the soft X-ray band ($E = 0.1$–0.4 keV), the hard band ($E = 0.4$–2.4 keV), and the hardness ratio (defined as the ratio of the hard over the soft band).

In order to investigate the possible variability in the X-ray light curve, we fitted the data with the average flux (indicated with the dashed line in Fig. 10). The statistical results are listed in Table 7. A constant flux is acceptable for all three energy

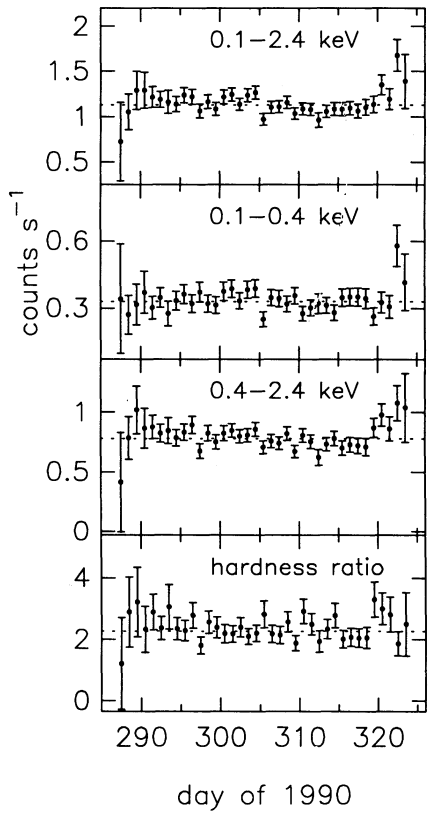

FIG. 10.—Light curves obtained with the *ROSAT* PSPC during the All Sky Survey. Note the absence of significant variability. Fit statistics are given in Table 7.

bands and the hardness ratio, as reflected by $\chi^2_{red} \lesssim 1.3$ and $q \gtrsim 0.1$ (q, the goodness-of-fit parameter, gives the probability that a chi-squared as large as the χ^2 listed in Table 7 is found by chance). All the light curves show a small negative slope, corresponding to a total decrease during the 37 day period of 8%, 6%, and 10% of the average count rate, for the total, soft, and hard light curve, respectively. But a straight line fit did not give lower reduced chi-squared values than in the constant count rate fit. We can therefore conclude that no significant variability is present in this data set. During the All Sky Survey the white dwarf KUV 18004+6836 was observed for 26 days. This white dwarf had a total count rate of 0.87 counts s^{-1}, almost as bright as H1821+643. Since 18004+6836 is a solitary white dwarf it can be used as a constant reference source. The statistics of its light curve are presented in Table 7. As its χ^2_{red} is similar but slightly higher than in the case of H1821+643, we can conclude that there was no intrinsic variability in the QSO on a time scale between one and 37 days during the period of observation.

TABLE 7

SHORT-TERM X-RAY LIGHT CURVE FIT

Band	Mean Count Rate (Counts s^{-1})	χ^2_{red}	q
Total	1.13	1.34	0.08
Soft	0.33	1.01	0.48
Hard	0.78	1.24	0.15
Hardness ratio	2.27	0.84	0.74
18004+6836[a]	0.87	1.46	0.06

[a] Total count rate of the reference source KUV 18004+6836.

This QSO was monitored for more than 200 days in 1977 with *HEAO A-1* in the 0.5–20 keV range (Snyder & Wood 1984). The error box of this detector is relatively small (0.05 deg^2; Wood et al. 1984) so that we can be certain that the detected emission originates in the QSO and not in any nearby sources. The planetary nebula K1−16 does not contribute in this energy range. Significant variability was found in the *HEAO A-1* light curve, as the flux changed by a factor of 2 on a time scale of about 10 days. H1821+643 was monitored with *EXOSAT* in 1985 during six monthly observations (Warwick et al. 1989). The ME count rate stayed approximately constant, while the count rate measured by the LE detector (with an energy range corresponding roughly to the hard band of the PSPC) decreased slowly by ~7% of the average flux per month.

4.2. *Long-Term X-Ray Variability*

Comparison of the flux around 1 keV as obtained with *Einstein* (KHSF) and *ROSAT* showed an increase of ~10% which is probably not significant. The new *Ginga* observations from 1990 are consistent both in slope and normalization with previous ones obtained in 1987 and 1988 (Kii et al. 1991). But a comparison of the *HEAO A-2* spectrum with the *ROSAT* spectrum, shows a drastic change. This cannot be explained by a contribution of K1−16 to the *HEAO A-2* spectrum, as the PSPC observations show that the white dwarf does not emit significantly in the 0.5–2.4 keV range of the LED detector of *HEAO A-2*. As discussed by KHSF, two SAO stars could be possible contributors to the soft X-ray flux. There is also a third weak source, KUV 18246+6508, close to the *HEAO A-2* error box. *ROSAT* observed these stars during the All Sky Survey and found the following fluxes in the observed 0.5–2.4 keV band (in ergs s^{-1} cm^{-2}): 9.97×10^{-13}, 3.11×10^{-12}, 8.80×10^{-13}, and 1.16×10^{-11} for SAO 17828, SAO 17878, KUV 18246+6508, and H1821+643, respectively. The flux observed with *HEAO A-2* in this band, derived from Pravdo & Marshall (1984), is 6.3×10^{-11} ergs s^{-1} cm^{-2}. Therefore, only one quarter of the flux observed by *HEAO A-2* in 1977 can be accounted for by the total flux observed with *ROSAT* in 1990 from the QSO and the three stars, and significant long-term variability seems to be present in the soft X-ray band. As the QSO and nearby stars have been observed repeatedly with no detection of large variability, one has to question the *HEAO A-2* observations rather than accept the fact that H1821+643 (or any of the stars near the error box) displayed a drastic change between 1977 and 1980 and remained constant ever since. Soft X-ray excesses in AGN are known to vary strongly (Elvis, Wilkes, & McDowell 1989), but the excess in the *HEAO A-2* spectrum is apparent up to $E \sim 2$ keV (§ 8) in contrast to the frequently observed soft excesses up to $E \sim 0.3$ keV. Only one QSO exhibits a soft excess up to ~2 keV (PG 1211+143), but although that soft excess has been found to vary in strength, the energy at which the soft and hard component intersect has not changed since 1979 (Elvis et al. 1991). In the absence of confirmation during the past 10 years, it is reasonable to doubt the reality of the strong soft X-ray emission detected with *HEAO A-2*.

4.3. *Short-Term UV Variability*

Seven SWP and LWP spectra were taken with *IUE* in 1990 October and November, approximately equally spaced in time

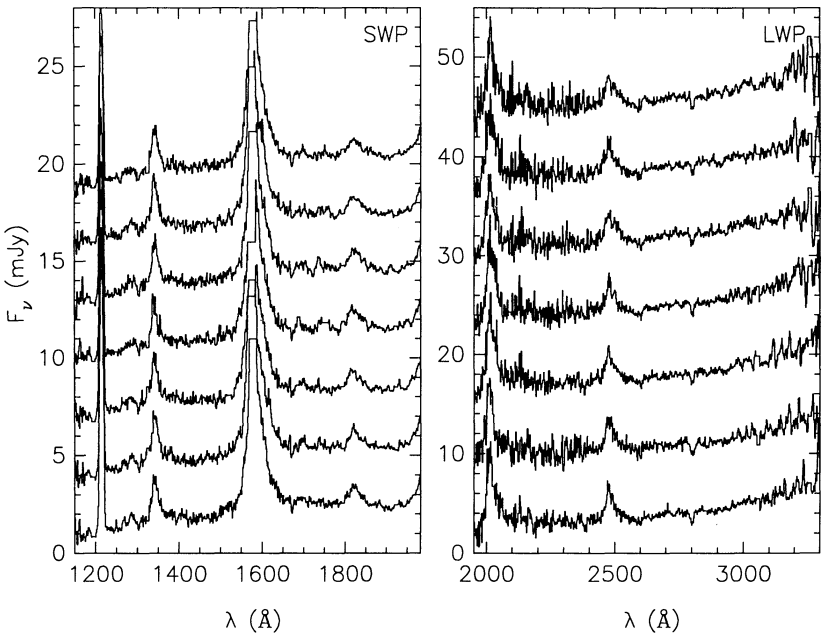

FIG. 11.—Individual spectra of H1821+643 obtained in 1990 October–November, before dereddening. Flagged data points are deleted. The spectra are displayed chronologically, with the first at the bottom and last at the top. The SWP and LWP spectra are offset by 3 and 7 mJy, respectively. Note the lack of significant changes from one spectrum to another.

and spanning a month all together. These spectra are shown in Figure 11. The data points seem to exhibit a slight modulation peaking around day 305, but if the error bars on the data points are taken into account, then it cannot be claimed that this modulation is significant. This is confirmed by a fit with the average flux (shown in Fig. 12 as the dashed lines and listed in Table 8). The error bars shown are the rms standard deviation from the mean in each continuum bin

$$\sigma_i = \left[\frac{\sum_{j=1}^{N} (f_j - \langle f \rangle)^2}{N-1}\right]^{1/2};$$

the exact uncertainties of the *IUE* data points are not known. These error bars might underestimate the true error as the uncertainty in the calibration is not taken into account, which is especially important below 1200 Å. Since we used the same calibration for all observations there should not be any contribution to the variability due the calibration. In Table 8 the second column gives the (error weighted) average flux

$$\left[\langle f \rangle = \left(\sum_{i=1}^{7} \frac{f_i}{\sigma_i^2}\right) \Big/ \left(\sum_{i=1}^{7} \frac{1}{\sigma_i^2}\right)\right],$$

the third column

$$\chi^2_{\rm red}\left[= \frac{1}{6}\sum_{i=1}^{7}\left(\frac{f_i - \langle f \rangle}{\sigma_i}\right)^2\right]$$

and the fourth column the goodness-of-fit probability q. Good fits could be obtained for all continuum wavelength intervals as the large q and small χ^2 values listed in Table 8 show. In the last column of Table 8 the upper limits to the variability as a percentage of the average flux are given. These upper limits are conservatively estimated from the 1 σ error estimates on the fluxes. At wavelengths where the sensitivity of the detector is highest (around 1890 and 2700 Å) the maximum variation is certainly less than 8% of the flux level on a time scale of 1 to 4 weeks. In summary, neither the continuum level nor the spectral shape was found to vary significantly during the one month monitoring with *IUE*.

TABLE 8

SHORT-TERM ULTRAVIOLET LIGHT CURVE FIT
(1990 October–November)

λ (Å)	$\langle f \rangle$ (mJy)	$\chi^2_{\rm red}$	q	Variability[a] (percent of $\langle f \rangle$)
1155–1190	2.45	0.09	0.997	38
1230–1250	2.82	0.09	0.997	20
1420–1495	3.59	0.12	0.995	13
1715–1790	4.63	0.52	0.795	10
1865–1915	4.64	0.39	0.888	8
2610–2780	6.50	0.12	0.994	8
2815–3000	7.12	0.21	0.973	11
α[b]	−0.95[b]	1.80	0.937	11

[a] Upper limit on the variability relative to $\langle f \rangle$.
[b] Power law index of the *IUE* (SWP + LWP) continuum fit ($F_\nu \propto \nu^\alpha$).

The flux ratio shortward and longward of the Lyman limit (redshifted to 1182 Å) did not vary significantly from the average (0.88 ± 0.13, where the error is the uncertainty in the flux ratio based on the σ's of the flux from the 1164–1182 and 1231–1254 Å continuum bins), implying a constant covering fraction of 12% ± 13%. A similar analysis for the co-added spectrum obtained in 1987 and 1989 suggests a slightly smaller covering fraction of 5% ± 10%.

4.4. *Long-Term UV Variability*

In KHSF we presented three sets of SWP and LWP spectra taken in 1987 and 1989 February and June. These data can be combined with the co-added spectrum obtained in 1990 October–November in addition to the archival observations

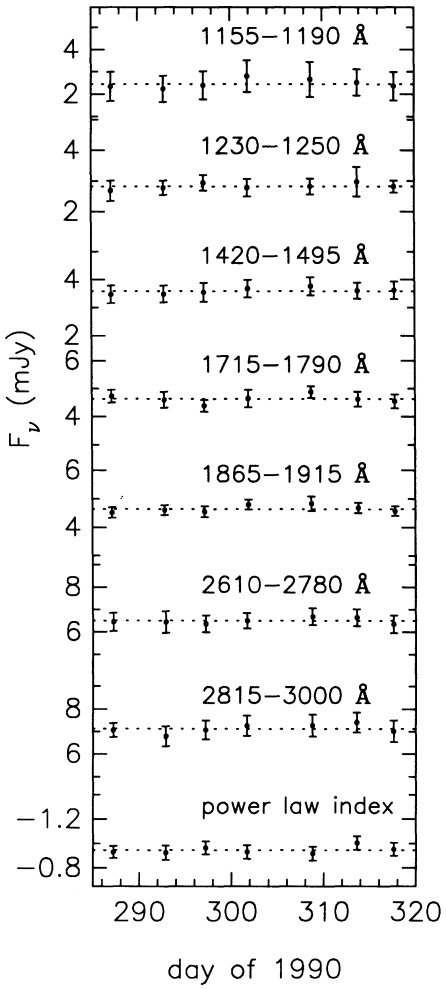

FIG. 12.—Short-term light curve of the ultraviolet continuum emission for the spectra obtained in 1990 October and November. The dashed line indicates the error-weighted average flux (listed in Table 8). Note the absence of significant variations for all wavelengths and the power-law index.

from 1990 July 24–25 (SWP 39299 and LWP 18439, with an integration time of 300 and 70 minutes, respectively) in order to study the long-term variability in the UV continuum. As shown in Figure 13, the 1987 July and 1989 February spectra did not change significantly in either flux level or spectral shape. The 1989 June and 1990 July observations differed significantly from all other spectra in spectral shape: the spectra were considerably harder. The 1990 October–November data showed the same spectral shape as found in 1987 and early 1989, but the overall flux level was ~20% lower than in early 1989 or before.

The sensitivity of the *IUE* detectors is known to degrade with time and we did not correct for this in our data reduction. For the LWP the change in sensitivity was (in the period 1985–1989) at most ~1% yr^{-1} (Teays & Garhart 1990). The SWP sensitivity decreased rapidly prior to 1980, but the most recent measurements (from 1984–1986, Bohlin & Grillmair 1988) showed variations similar to the LWP (except at higher wavelengths: ~2% yr^{-1} around 1950 Å). Therefore, we estimate that the contribution of the detector degradation to the change in flux level is at most ~2% out of the total of 20% between 1989 and 1990.

To investigate the significance of the variations, the four data points were fitted with the (error weighted) average flux (indicated by the dashed line in Fig. 13). The goodness-of-fit probability (q) is listed in Table 9, together with the average flux and χ^2_{red}. The continuum points around 1890 Å were most significantly variable with $q \sim 5 \times 10^{-8}$ and $\chi^2_{red} \sim 10$.

4.5. *Long-Term Optical Variability*

Of the optical spectra listed in Table 4 we discuss the ones obtained contemporaneously with the *IUE* observations here. These spectra are remarkably similar with a maximum variation of 6%. This variability is small but probably significant. Compared to the spectrum obtained on 1990 October 20, some spectra differ only photometrically (e.g., in the spectrum obtained on 1990 November 11 the flux level is about 2% higher), while others have different spectral slopes (Fig. 14). The continuum slope between 5000–8000 Å, which is representative of the true continuum (as blended Fe II lines and Balmer

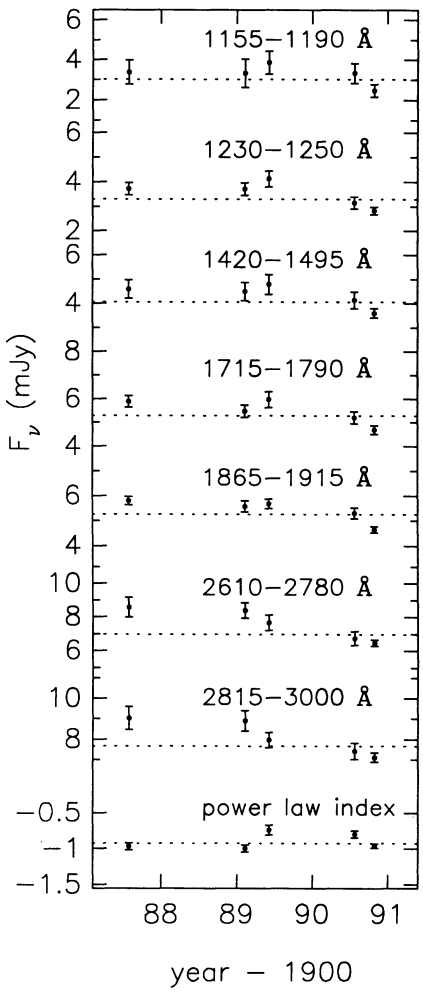

FIG. 13.—Long-term light curve of the ultraviolet continuum emission for the spectra obtained between 1987 and 1990. The dashed line indicates the error-weighted average flux (listed in Table 9). Note the absence of change between 1987 and early 1989 and the significant change in spectral shape during 1989: the spectrum hardened as reflected by the higher fluxes in the short-wavelength continuum bands, the lower fluxes in the long-wavelength continuum bands, and the increase in the power-law index. The 1990 continuum flux is consistently lower than the previous observations.

TABLE 9

LONG-TERM UV LIGHT CURVE FIT (1987–1990)

λ (Å)	$\langle f \rangle$ (mJy)	χ^2_{red}	q
1155–1190	3.02	1.50	2.0×10^{-1}
1230–1250	3.30	5.23	3.3×10^{-4}
1420–1495	4.05	3.08	1.5×10^{-2}
1715–1790	5.29	5.25	3.2×10^{-4}
1865–1915	5.26	9.90	5.2×10^{-8}
2610–2780	6.96	6.48	3.3×10^{-5}
2815–3000	7.67	4.60	1.0×10^{-3}
α[a]	−0.92[a]	17.7	1.4×10^{-3}

[a] Power-law index of the *IUE* (SWP + LWP) continuum fit ($F_\nu \propto \nu^\alpha$).

continuum emission contribute shortward of ~5000 Å), is similar ($\alpha = 0.37$) for the spectra obtained in 1988 October (KHSF) and in 1990 October, while the spectrum obtained in 1990 July had a much steeper rising slope ($\alpha = 0.54$). The continuum spectrum obtained at Palomar had the same flat slope longward of 5000 Å, but showed $\lesssim$6% change from the spectrum obtained on 1990 October 20 at shorter wavelengths. This variability could possibly be attributed to the Fe II blended line emission. The flat slope in 1988 and 1990 October–November, and the steep slope in 1990 July, are consistent with the change in the spectral slope in the UV (Fig. 13);

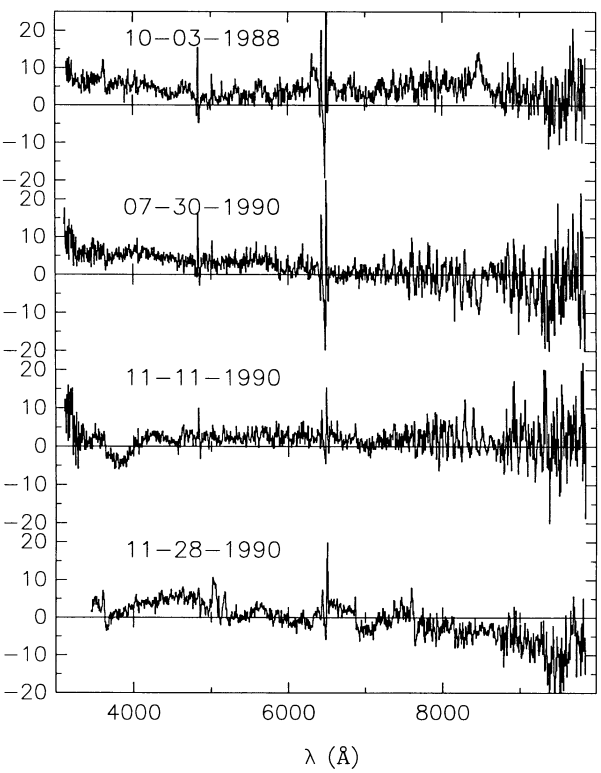

FIG. 14.—Difference spectra as function of wavelength. Shown is the spectrum, indicated by the date of the observation, minus the spectrum obtained on 1990 October 20 (in % of the flux of the latter spectrum). Note that the variations in the continuum are generally small ($\lesssim$6%). Notice also that the 1990 July 30 difference spectrum does not show any significant variations longward of 6500 Å while it differs significantly below that wavelength. The bump shortward of 4000 Å in the 1990 November 11 difference spectrum is probably due to the calibration.

both in the UV and optical the slope increased by ~0.16. In summary, the spectra vary in flux and shape, but the change is never more than 6%.

5. EMISSION LINES

Information on continuum emission in the unobservable extreme ultraviolet gap can be derived from the UV and optical emission lines, which are powered by photons with EUV energies. To this end, we measured the major emission lines in the UV and optical spectra. No significant differences in line fluxes were found from one *IUE* observation to the other in 1990; therefore, all the *IUE* spectra were co-added. The optical lines were measured in the moderate-resolution spectrum obtained at Palomar. The measured line properties are listed in Table 10 and the lines are identified in Figures 2 and 5. The Lyman-α emission line could not be measured, as all spectra were saturated at this line, and we listed the value obtained in 1987 in Table 10. The major source of error in the line measurements is the uncertainty in the continuum level, which is contaminated by the broad wings of the emission lines, Galactic absorption lines, and blended Fe II line and Balmer continuum emission.

With the long exposures times of these *IUE* spectra, caution should be taken with the possible presence of camera artifacts which mimic emission features. Using the reference artifact spectrum published by Crenshaw, Bruegman, & Norman (1990), we identified the following probable camera artifacts in the co-added spectrum: at 1280 and 1290 Å with an expected dereddened flux of 0.5 mJy, around 1665 Å (shortward of the Al II absorption line) with an expected dereddened flux of 0.6

TABLE 10

EMISSION-LINE MEASUREMENTS OF H1821+643

ID[a]	Intensity[b]	Flux[c]	EW[d]
C III λ977	<39.4	<28.1	<7.5
O VI λ1034[e]	125.0	92.4	20.4
Lyα λ1216, (N V λ1240)[f]	963.5	626.9	156.0
Si IV λ1397, O IV λ1407	48.1	38.6	11.8
C IV λ1549	500.0	368.4	145
C III] λ1909	94.2	77.2	32.4
Mg II λ2798	217.3	182.1	100.1
O III λ3133	1.5	1.3	0.8
[Ne V] λ3345	2.2	1.9	1.3
[Ne V] λ3426	4.6	4.0	2.9
[O II] λ3727	5.9	5.3	4.6
[Ne III] λ3869, Hζ λ3889, He I λ3888	13.7	12.5	12.8
Hε λ3970, [Ne III] λ3968	6.2	5.7	6.5
Hδ λ4102	9.3	8.8	11.3
Hγ λ4340, [O III] λ4363	27.6	26.5	37.2
He II λ4686	0.8	0.8	1.3
Hβ λ4861	100.0	100.0	185.7
[O III] λ4959	6.4	6.4	11.4
[O III] λ5007, (Fe II)	27.7	27.5	50.8
He I λ5876	8.6	8.9	22.0
[O I] λ6300	1.0	1.1	2.8
[O I] λ6363	0.4	0.4	1.0
Hα λ6563, ([N II] λλ6548, 83)	314.4	332.3	952.0
[S II] λ6716, 30, (He I λ6678)	2.9	3.0	9.6

[a] Identification of emission line and rest wavelength; the lines in parentheses denote only minor contributions.

[b] Intensity corrected for Galactic reddening, relative to Hβ, with $I(H\beta) = 1.04 \times 10^{-12}$ ergs cm^{-2} s^{-1}.

[c] Observed flux relative to Hβ with $F(H\beta) = 8.55 \times 10^{-13}$ ergs cm^{-2} s^{-1}.

[d] Observed equivalent width in Å.

[e] Narrow component only (FWZI ~40 Å).

[f] Measurement from 1987 (KHSF).

mJy, and possibly the bump of emission around 1740 Å with an expected dereddened flux of 0.5 mJy.

For the O VI λ1034 emission line only the narrow component was measured (with a full width near zero intensity, FW0I, of ~40 Å), as it was unclear how far the broad wings extend (possibly from 1260 to ~1400 Å). The blue wing of O VI is especially difficult to determine due to the possible presence of C III around 1270 Å, the likely presence of the camera artifacts around 1280 and 1290 Å, and the absorption line around 1300 Å. This uncertainty around the O VI line also complicates the measurement of the upper limit to C III λ977, as well as the measurement of the O I λ1302, Si II λ1304 absorption feature. A high-resolution spectrum obtained with the *HST* FOS showed only evidence for the narrow component of the O VI line (Bahcall et al. 1992), while no C III emission was detected.

These 1990 UV line measurements can be compared to the ones obtained in 1987 and 1989. The flux measurements did not change significantly. The equivalent widths increased on average by ~20%, which could be accounted for by the lower overall continuum level. Likewise, no significant changes occurred in the optical line strengths between 1988 and 1990. Small but significant differences are found for the blended Fe II emission, e.g., the feature around 3850 Å decreased while an increase was found around 4550 Å. The optical spectrum obtained in 1990 at Palomar had considerably better spectral resolution and the line measurements (especially of the [O I] lines) are therefore preferred over the ones listed in KHSF. The observed line ratios in H1821+643 are consistent with a power-law plus disk spectrum peaking at 10 eV (i.e., in the UV), within the context of the Krolik & Kallman (1988) model; this is similar to the conclusion reached in KHSF.

6. UV ABSORPTION LINES

We measured the absorption lines listed in Table 11 and indicated by tick marks in Figure 2. The lines are from Galactic low-ionization species (except for C IV for which only an upper limit is obtained due to its location on the blue wing of Lyman-α). There are possible absorption lines present of Si IV λ1394 and Al III λ1855 with equivalent widths of about 0.5 and 0.3 Å, respectively, but these lines are too weak to allow for definite detection. Bahcall et al. (1992) did not claim the detection of the Al III line although there is marginal evidence for it in their FOS spectrum. Compared with the measurements in 1987 and 1989, the equivalent widths of the absorption lines observed in 1990 are similar, with the exception of the Al II and several Fe II lines. The 1990 measurements are to be preferred as they are based on the co-added spectrum with a much higher signal-to-noise ratio. We did not detect any absorption lines in the optical spectrum.

TABLE 11

ABSORPTION-LINE MEASUREMENTS OF H1821+643

ID[a]	EW (Å)
S II λ1251, 1254, 1260, Si II λ1260	0.8 ± 0.2
O I λ1302, Si II λ1304	1.8 ± 0.2
Lyα λ1216 (z = 0.225 ± 0.002)	0.6 ± 0.2
Si II λ1527	0.4 ± 0.1
C IV λ1548, 51	<0.8 ± 0.2
Al II λ1671	1.3 ± 0.1
Fe II λ2343	0.8 ± 0.4
Fe II λλ2374, 2382	1.6 ± 0.2
Fe II λ2586	1.3 ± 0.2
Fe II λ2599	1.8 ± 0.2
Mg II λ2796, 2803	3.6 ± 0.2

[a] Identification of absorption line and rest wavelength.

The spectral region shortward of the Lyman-α emission line allows the detection of low-redshift Lyman-α forest lines. In the co-added spectrum of 1987 and 1989 we detected two absorption features around 1470 and 1490 Å, with EW = 0.7 ± 0.2 Å and 1.0 ± 0.2 Å, respectively (with the error given being formal). In the co-added data obtained in 1990 (Fig. 2), we detect only a feature at 1489 ± 2 Å (EW = 0.6 ± 0.2 Å). Since the 1990 data have better signal-to-noise ratio, we consider only the feature at 1489 Å significant. Bahcall et al. (1992) also detected this absorption feature at 1489.35 Å. There are no Galactic absorption features expected at this wavelength. Schneider et al. (1992) found a foreground galaxy at z = 0.226. This redshift is consistent with a Lyman-α absorber at 1489 Å as observed in the *IUE* and *HST* spectra. The projected separation between the foreground galaxy and the QSO is 173 kpc. This might be quite large to attribute the UV absorption to the galaxy, but it is not unprecedented; Salzer (1992) found a possible association between a low z Lyman-α cloud (along the line of sight to 3C 273) and a galaxy separated by 415 kpc.

In the case of 3C 273 *HST* detected 14 Lyman-α forest lines in the redshift range 0.016–0.151 (Morris et al. 1991; Bahcall et al. 1991). This surprising result indicates a flattening of the evolution of the absorbers, so that the comoving number density is roughly constant between z = 2 and z = 0. Two of the lines in 3C 273 have equivalent widths of ~0.3 Å (Morris et al. 1991), so it is reasonable that one Lyα line has been detected in the co-added *IUE* spectrum of H1821+643. Bahcall et al. (1992) detected in the *HST* spectrum of H1821+643 ten extragalactic Lyman-α absorption lines (in the 0.122–0.297 redshift range) and three Lyman-β lines, in addition to absorption lines associated with the QSO itself (or the cluster around it). In contrast to the Lyman-α forest lines detected at large redshifts, the Lyman-α lines in the H1821+643 spectrum appear to be correlated like galaxies, and this, in addition to the identification of at least one of the absorbers with an intervening galaxy, suggests that their origin is not truly intergalactic.

The spectral region between Lyman-α and C IV λ1549 covers the redshift range 0.04–0.27 for detection of C IV absorption lines. In this sensitive part of the SWP camera no such absorption features were found above the detection threshold of EW ~0.2 Å. Intergalactic C IV lines are not expected for the low redshift of H1821+643 (Bergeron 1988). Bahcall et al. (1992) did not detect any absorption features in this wavelength range either. These authors did, however, detect absorption lines superposed on the emission lines of C IV and also of O VI and Lyman-α, which had never been detected in a low-redshift QSO and were notably absent in the *HST* spectrum of 3C 273 (Bahcall et al. 1991).

7. OPTICAL COLORS

In this section we show that H1821+643 is more likely a blue than a red QSO as suggested by HN. These authors obtained photometry of H1821+643 in the B and R bands in 1989 and in the V and I band in 1990. They claimed for the QSO nucleus that $B-R$ = 1.1 and $V-I$ = 1.3, from which they concluded that the QSO is remarkably red due to intrinsic

reddening [with $E(B-V) = 0.5$], as the typical $B-R$ range for infrared bright QSOs is 0.1–0.7 (HN).

To check their results, we calculated the colors from our spectra obtained contemporaneously with the *IUE* observations and under photometric conditions. These "spectroscopic colors" of 1988 were consistent with the photometry obtained in 1988 (KHSF). The change in color between 1988 October and 1990 October was small: 0.04, 0.03, and 0.04 mag in the B, V, and R bands, respectively. The $B-R$ color remained unchanged between 1988 October and 1990 October at about -0.16 [after correction for the Galactic extinction with $E(B-V) = 0.085$], which is consistent with the constancy of the spectral slope (§ 4.5). Although we cannot exclude variability, the small differences between the colors in 1988 and 1990 suggest otherwise. The spectra with a slightly different slope (e.g., obtained at 1990 November 11 and July 30) were steeper, leading to an even lower $B-R$ (of about -0.21). The comparison of these "spectroscopic" colors to the photometry presented by HN might be somewhat uncertain due to the possibly different transmission curves and normalizations used, but that could not explain the discrepancy of at least 1.2 mag. The small "spectroscopic" $B-R$ is indicative of a blue rather than a red object. The blue color of H1821+643 is consistent with the strong optical/UV bump which indicates very little internal reddening. Also, the good agreement between the absorption column indicated by the 21 cm observations and the various X-ray measurements, suggests that internal reddening is not significant. Moreover, if the color excess were 0.5 mag as claimed by HN, then a very strong 2200 Å dust feature should probably be present around 2900 Å, and the dereddened emission line ratios would be unusual. However, no such dust feature is present in the *IUE* spectra (Fig. 2) and the line ratios are very typical for a QSO (Table 10; see also KHSF).

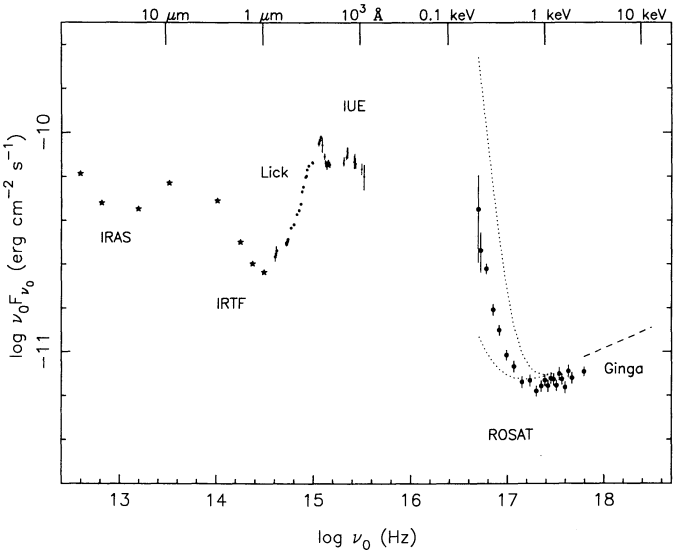

FIG. 15.—Continuum energy distribution plotted in the QSO rest frame, with the co-added *IUE* data from 1990 October–November, the co-added *ROSAT* spectrum during the RASS (the spectral model is discussed in § 3.3; the contribution from K1−16 has been subtracted), the average *Ginga* spectrum from 1990 October, the optical spectrum obtained on 1990 October 20 at Lick Observatory, in addition to published *IRAS* and IRTF data. The X-ray data have been corrected for interstellar absorption (with $N_H = 4.1 \times 10^{20}$ cm^{-2}), while all the other data have been corrected for intersteller extinction [with $E(B-V) = 0.085$ mag]. The dotted lines indicate the error introduced by the range of possible slopes of the soft X-ray excess.

8. CONTINUUM ENERGY DISTRIBUTION

In Figure 15 we present the first simultaneous continuum energy distribution (CED) from 1 μm up to 10 keV, complemented by published infrared photometry (Neugebauer et al. 1986; KHSF). The CED is shifted into the rest frame of the QSO as denoted by ν_0 (while ν, λ, or E refers to the observed frame). We corrected the X-ray data points for interstellar absorption by the Galactic column density, and corrected the other data points for interstellar extinction with $E(B-V) = 0.085$. These data are also listed in Table 12. The near- and far-infrared points are not simultaneous, but match up well with the optical data from 1990. As the amplitude of the variability in AGNs is found to decrease with increasing wavelength (Cutri et al. 1985) and since the optical variability is less than 6%, the change in the infrared ($\lambda > 1$ μm) is expected to be insignificant.

9. DISCUSSION

9.1. *Radio to Infrared Emission*

The radio spectral index as defined by the fluxes at 6 and 20 cm is $\alpha_{6,20\,cm} = -0.89$ ($f_\nu \propto \nu^\alpha$), a typical value for a radio quiet QSO (RQQ; Barvainis & Antonucci 1989; Chini, Kreysa, & Biermann 1989). This spectral steepness, together with the resolved image, supports the interpretation of the radio emission as extended optically thin synchrotron radiation (Barvainis & Antonucci 1989). Some caution should be exercised because of the almost 2 year time period between the radio observations, although strong variability on such a time scale is only expected for compact cores. The flux is rather high for a RQQ but still a factor of 50 smaller than in a typical radio loud QSO (Kellerman et al. 1989). With the northern radio component (Fig. 3*b*) being nearly coincident with the optical position of H1821+643, the weaker component 2″ to the south could be associated with the host galaxy of the QSO (which has an optical radius of at least 5″; HN) or a foreground galaxy. The radio image seems to suggest that the two radio components are connected and indicate therefore that they both originate in the QSO, although it cannot be ruled out that the weaker component arises in a foreground galaxy.

The short wavelength *IRAS* points and the near-infrared points show a strong near-infrared (or 5 μm) bump, generally attributed to nuclear optical/UV continuum radiation reprocessed by warm dust (Barvainis 1987). A parabolic fit peaks around 7 μm. The observed upturn at the long wavelength *IRAS* points (sometimes called the far-infrared excess) is commonly thought to arise in cool dust from the Galactic disk (Barvainis 1990). Whether this explanation is valid for such a high-luminosity QSO as H1821+643 is questionable, as it requires an enormous amount of dust to account for an energy output similar to the nuclear near-IR and optical/UV emission. HN measured the optical diameter of the host galaxy to be 160 kpc, which is very large for any galaxy and could possibly account for the strong far-infrared excess. The upper limit to the 1.3 mm flux quoted by Chini et al. (1989) is not valid, and cannot be used to address the origin of the far-infrared emission, since they observed at the incorrect position given by Pravdo & Marshall (1984).

TABLE 12

CONTINUUM ENERGY DISTRIBUTION OF H1821+643

log ν_0 (Hz)	log $\nu_0 f_{\nu_0}$ [a] (ergs cm^{-2} s^{-1})	log ν_0 (Hz)	log $\nu_0 f_{\nu_0}$ [a] (ergs cm^{-2} s^{-1})
14.604.....	−10.566	15.316.....	−10.125
14.620.....	−10.538	15.341.....	−10.111
14.719.....	−10.503	15.346.....	−10.084
14.724.....	−10.509	15.352.....	−10.090
14.728.....	−10.500	15.419.....	−10.134
14.733.....	−10.496	15.426.....	−10.117
14.738.....	−10.485	15.434.....	−10.141
14.768.....	−10.434	15.495.....	−10.166
14.799.....	−10.419	15.520.....	−10.200
14.828.....	−10.371	16.697.....	−10.350
14.859.....	−10.354	16.723.....	−10.538
14.869.....	−10.324	16.783.....	−10.621
14.882.....	−10.266	16.854.....	−10.808
14.895.....	−10.246	16.916.....	−10.902
14.918.....	−10.202	16.991.....	−11.015
14.926.....	−10.197	17.067.....	−11.067
14.933.....	−10.168	17.151.....	−11.139
14.948.....	−10.151	17.233.....	−11.131
14.992.....	−10.137	17.299.....	−11.180
15.055.....	−10.050	17.350.....	−11.157
15.065.....	−10.035	17.388.....	−11.130
15.076.....	−10.022	17.420.....	−11.156
15.091.....	−10.057	17.450.....	−11.121
15.116.....	−10.108	17.477.....	−11.126
15.123.....	−10.139	17.508.....	−11.154
15.129.....	−10.143	17.536.....	−11.101
15.136.....	−10.148	17.565.....	−11.126
15.149.....	−10.140	17.598.....	−11.164
15.156.....	−10.137	17.631.....	−11.090
15.162.....	−10.145	17.670.....	−11.119
15.169.....	−10.145	17.794.....	−11.092
15.310.....	−10.140	17.797.....	−11.024
		18.496.....	−10.891

[a] After correction for interstellar absorption with $N_H = 4.1 \times 10^{20}$ cm^{-2} (for the X-ray data) or Galactic extinction with $E(B-V) = 0.085$ (for all the other data), and after subtraction of the contribution from K1−16 (in the ultrasoft X-ray band).

9.2. *Optical to X-Ray Emission*

As discussed previously in KHSF, the optical/UV bump is very pronounced. The slope of the optical continuum (between $\lambda \sim 5000$ and 8000 Å) is 0.37 ± 0.02, while the UV slope is remarkably flat ($\alpha \sim -0.95 \pm 0.03$, with a flux level of log $\nu_0 f_{\nu_0} \sim -10.2$). There is a downward trend in the SWP data points ($\alpha \sim -1.11 \pm 0.10$), indicating the presence of a turnover in the UV. This turnover occurs around log $\nu_0 = 15.35$ ($\lambda \sim 1700$ Å; the frequencies are given in Hz here and throughout the remainder of this article).

The soft X-ray data points deviate strongly from the power-law below ~0.3 keV. This soft X-ray excess is steep with $\alpha \sim -4.13 \pm 0.96$, reaching up to log $\nu_0 f_{\nu_0} \sim -10.3$ at log $\nu_0 = 16.7$ ($E = 0.16$ keV). The fit with a blackbody model to the soft excess (§ 3.3) resulted in a best-fit value of $kT = 40$ eV with an upper limit of 68 eV, corresponding to $T = 5 \times 10^5$ K and 8×10^5 K, respectively. Compared to the sample of QSOs studied with low-resolution detectors on board *EXOSAT* (Comastri et al. 1992), the power-law slope is rather steep and the blackbody temperature low, but neither are strongly different from the sample's average values. The X-ray spectrum of *ROSAT* joins the *Ginga* observations well. The energy index as measured by *ROSAT* (in the three component fits) is 0.81 ± 0.05, while *Ginga* found 0.78 and 0.83 for the two observations. These indices are very typical for a high-luminosity AGN (Williams et al. 1992). The *Ginga* spectrum of H1821+643 displays a strong Fe II line (EW = 210 ± 80 eV; Kii et al. 1991) which could in part be attributed to the cluster around the QSO as Schneider et al. (1992) found that H1821+643 is located in a dense cluster. Such a cluster might also contribute to the X-ray continuum emission. However, Kii et al. did not find any spectral evidence for thermal bremsstrahlung from such a cluster medium and concluded that the strong Fe II line is intrinsic to the QSO. With an angular radius of $\lesssim 50''$ (Schneider et al. 1992) the cluster contribution, if any, is too small to be resolved with the PSPC in scanning mode.

In order to present the intrinsic emission from the QSO we subtracted the contribution of the white dwarf (i.e., the blackbody spectral component) from the PSPC spectrum. The contribution from K1−16 is rather uncertain as reflected by the large errors on the normalization and blackbody temperature (§ 3.3.). In the best-fit models K1−16 and the soft excess of H1821+643 contribute equally to the count flux around 0.14 keV, while the white dwarf's contribution declines above that energy. For that reason we could only study the intrinsic emission from the QSO above 0.16 keV ($\lambda = 80$ Å, log $\nu_0 = 16.70$).

As the absorption by interstellar hydrogen is quite high at these low energies, even for the moderate absorption column of 4.1×10^{20} cm^{-2}, any uncertainties in N_H will lead to large errors in the unabsorbed flux. Typically a 10% uncertainty in the column density will produce a 30% error in the flux at 0.2 keV. Although there cannot be any doubt that there is a soft X-ray excess present in the intrinsic QSO spectrum, its strength and spectral shape are difficult to determine with certainty as reflected by the large errors on the fit parameters of the soft excess in § 3.3. The possible range of the soft X-ray excess due to the error on the slope is shown in Figure 15 by the dotted lines. The errors on the *ROSAT* data points only reflect the statistical uncertainty. The soft X-ray excess ($E < 0.5$ keV) will therefore be rather uncertain and this should be kept in mind when interpreting the soft excess and its connection with emission in other wavelength bands.

9.3. *Accretion Disk Models*

From multiwavelength variability studies of AGNs (e.g., Cutri et al. 1985) it has been established that the optical/UV bump is a separate component in the CED. Likewise, the soft X-ray excess varies independently from the hard X-ray emission (Elvis, Wilkes, & McDowell 1989, and references therein). As both components have been attributed to an accretion disk, we discuss the applicability of simple thin disk models in the case of H1821+643.

It is well known that around 3000 Å Balmer continuum and blended Fe II lines form a pseudo-continuum (Wills, Netzer, & Wills 1985) that should not be attributed to the emission from an accretion disk. The data points in the near-UV range (log $\nu_0 \sim 14.9$–15.1) are therefore expected to exceed the predicted accretion disk emission. More important is the power-law ranging from the infrared to the hard X-ray bands which is assumed to exist in addition to the accretion disk emission. This power-law was invoked because Edelson & Malkan (1986) claimed a strong IR–X-ray correlation, but its existence has since been disputed (e.g., Sanders et al. 1989). Alternatively, the infrared emission could be fitted with thermal dust models. These models will not contribute much above 1 μm and can be neglected above log $\nu_0 \sim 15.2$. Also, the IR–X-ray power-law could be truncated at optical frequencies (Czerny & Elvis 1987)

and again no contribution will be made above log $\nu_0 \sim 15.2$. The use of these models rather than the IR–X-ray power-law (typically with $\alpha \sim -1.2$) will result in a slightly different spectral slope for the total (power-law plus accretion disk) emission and also change the parameters of the disk model (M, $\dot{M}$, and the outer radius). While bearing this uncertainty in mind, we will nevertheless present accretion disk models plus the IR–X-ray power-law, in order to compare the model parameters with KHSF.

We calculated the luminosities in the optical, UV, and soft X-ray band and found (in ergs s^{-1}): 1.8×10^{46}, 2.3×10^{46}, and 1.9×10^{46}, respectively, adding up to a minimum luminosity in the optical/UV/X-ray bump of $L_{\rm min} = 6.0 \times 10^{46}$. This $L_{\rm min}$ can be related to a minimum accretion rate through $\dot{M}_{\rm min} = L_{\rm min}/c^2\eta$, with η being the efficiency for accretion ($\eta \sim 6\%$ in the Newtonian metric). This leads to $\dot{M}_{\rm min} \sim 18\ M_\odot\ {\rm yr}^{-1}$. If we estimate the luminosity in the unobservable EUV gap by a straight line connecting the *ROSAT* and *IUE* points, then $\dot{M} \sim 40\ M_\odot\ {\rm yr}^{-1}$.

Following Bechtold et al. (1987) we applied a simple sum-of-blackbodies model for an optically thick, physically thin accretion disk. Such a model is independent of the viscosity parameter. In Figure 16 (*left panel*) we show a Newtonian accretion disk model with $M = 3 \times 10^9\ M_\odot$, $\dot{M} = 15\ M_\odot\ {\rm yr}^{-1}$ and $R_{\rm out}/R_{\rm in} = 12$ (where $R_{\rm in} = 3R_{\rm Sch}$; the inclination angle i is such that $\cos i = 0.5$). The luminosity is sub-Eddington ($L/L_{\rm Edd} = 0.13$). The $R_{\rm out}/R_{\rm in}$ ratio is exceptionally small as discussed in detail in KHSF. Such a fit, peaking at UV frequencies, does not contribute above log $\nu_0 = 16$, thus failing to fit the X-ray excess (even the lower limit to the soft excess). In KHSF a similar fit produced the same parameters except for $\dot{M}$ which was $19\ M_\odot\ {\rm yr}^{-1}$, which could be accounted for by the $\sim$20% higher flux level in 1987 compared to 1990.

If the reality of the turnover in the UV is doubted, then the spectrum could turn over at higher frequencies but below the lowest frequency of the soft excess, thus log $\nu_{\rm max} \leq 16.7$. Such a fit in the Newtonian metric would result in highly super-Eddington luminosities ($L/L_{\rm Edd} \gtrsim 20$). This could be mitigated by considering accretion disk models around a rapidly rotating black hole viewed close to the plane of the disk (e.g., Sun & Malkan 1989). The efficiency η is much higher in the Kerr metric. In this case it is necessary to include the relativistic effects which lead to focusing of the most energetic photons along the disk, thus resulting in harder spectra at high inclination angles (Cunningham 1975). It is for this reason that QSOs with strong soft X-ray excesses are thought to have nearly edge-on accretion disks. In Figure 16*b* a fit with the following fit parameters is shown: $M = 10^8\ M_\odot$, $\dot{M} = 2.5\ M_\odot\ {\rm yr}^{-1}$, and $\cos i = 0.25$, resulting in $L/L_{\rm Edd} \sim 3$ which is moderate compared to the luminosity in the Newtonian metric and will not violate the thin disk approximation in the inner regions significantly.

Such a fit peaking close to log $\nu_0 \leq 16.7$ would represent the soft excess well (Fig. 16*b*). In fact, its steep slope ($\alpha \sim -4$), is consistent with the high-energy tail of the disk emission, in contrast to the soft excess in PG 1211+143 with $\alpha = -2.2$, which could only be fit successfully after introducing Comptonization (Bechtold et al. 1987). However, these fits with maxima in the soft X-ray band do not match the emission in the UV, either strongly underestimating the observed optical/UV emission, or resulting in much steeper (positive) spectral slopes than the observed $\alpha_{\rm swp} \sim -1.1$ in the UV. The latter is shown in Figure 16*c*, where $M = 7 \times 10^8\ M_\odot$, $\dot{M} = 18\ M_\odot\ {\rm yr}^{-1}$, $\cos i = 0.75$, and $L/L_{\rm Edd} \sim 6$, resulting in a good fit to the optical data points, a reasonable fit to the soft X-ray data (the slope is about -5, similar to the upper limit of the soft excess), and a failure to fit the UV data.

As inclusion of relativistic inclination effects will only shift the disk spectrum to different energies rather than changing the spectral slope in the UV (Sun & Malkan 1989), it does not solve the problem of the discrepancy between these fits and the observed optical/UV bump. Only the edge-on solution has a significantly different spectral shape, but with an even steeper spectrum (i.e., with a more positive α) at ultraviolet wavelengths. One might expect that the size of the disk influences the broadness of the bump and the steepness of the fit in the UV. However, a substantial increase of the outer radius hardly changes the emerging disk spectrum as the outer radii do not contribute strongly to the disk emission (Bechtold et al. 1987). Therefore, the spectral slope will decrease slightly but certainly not enough to fit to the observed UV data points (as illustrated in Fig. 16*b* where we increased $R_{\rm out}/R_{\rm in}$ from 50 to 200 with only minor effect). Furthermore, disks with too large outer radii could be gravitationally unstable (Bechtold et al. 1987).

Therefore, the simple sum-of-blackbodies models cannot fit both the optical/UV bump and the soft X-ray excess. These models predict a slope in the optical/UV range around $\frac{1}{3}$, unless the fit peaks in the UV, but then it fails in the soft X-ray band. This conclusion can be drawn in the case of H1821+643 because of its optimal redshift. Higher redshift objects will suffer significantly from absorption due to intervening Lyman-α clouds, while lower redshift QSOs do not allow for good coverage of the UV bump within the bandpass of *IUE* (or *HST*). The latter is the case for the low z object PG 1211+143 (Bechtold et al. 1987), which only displays the $\alpha \sim \frac{1}{3}$ rise and in which a possible turnover at log $\nu_0 = 15.35$ could not have been detected. Without such a turnover (or $\alpha \sim -1$ slope in the UV), disk model fits are far less constrained, and it is not surprising that acceptable fits were obtained in the case of PG 1211+143.

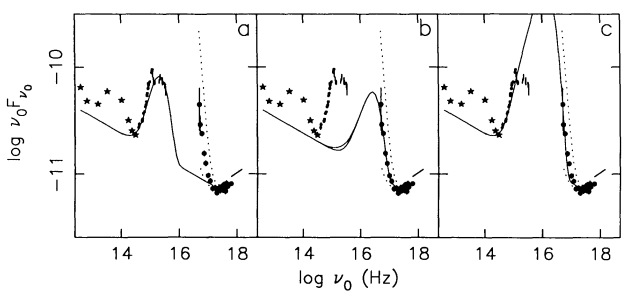

FIG. 16.—Overall continuum spectrum of H1821+643 plotted in the QSO rest frame (same data and units as in Fig. 15) with accretion disk model fits (*solid line*). Deviations between log $\nu_0 = 14.9$ and log $\nu_0 = 15.1$ are due to the Balmer continuum and Fe II line emission. (*a*) Newtonian disk model in addition to power law ($\alpha = -1.16$) with $M = 3 \times 10^9\ M_\odot$, $\dot{M} = 15\ M_\odot\ {\rm yr}^{-1}$, $R_{\rm out}/R_{\rm in} = 12$, $\cos i = 0.5$, $R_{\rm in} = 3R_{\rm Sch}$. $L/L_{\rm Edd} = 0.13$. (*b*) Kerr disk model in addition to power law ($\alpha = -1.16$) with $M = 10^8\ M_\odot$, $\dot{M} = 2.5\ M_\odot\ {\rm yr}^{-1}$, $\cos i = 0.25$, $R_{\rm in} = 0.62R_{\rm Sch}$. $L/L_{\rm Edd} = 3.1$. The substantial increase of the outer to inner radius ratio from 50 (*lower curve*) to 200 (*upper curve*) does not improve the fit to the optical/UV bump significantly. (*c*) Kerr disk model in addition to power law ($\alpha = -1.16$) with $M = 7 \times 10^8\ M_\odot$, $\dot{M} = 18\ M_\odot\ {\rm yr}^{-1}$, $R_{\rm out}/R_{\rm in} = 200$, $\cos i = 0.75$. $L/L_{\rm Edd} = 5.7$. Notice the good fit to the optical data, the reasonable fit to the soft excess and the failure to fit in the UV.

Inclusion of scattering effects in the disk model might change the spectral shape above log $\nu_0 \sim 15.3$ (Czerny & Elvis 1987). Comptonization has an adverse effect on the slope: it will steepen the slope at soft X-ray energies (i.e., α will be more negative) and reduce the slope somewhat at UV frequencies (i.e., α will be more positive), thus widening the gap between the model and the data points even further. Electron scattering opacity could possibly contribute to the flat slope observed in the UV. This should be addressed by comprehensive accretion disk models incorporating radiative transfer of the disk emission in a consistent manner (as an accurate description is required of the disk density as a function of radius in order to describe the opacity coefficients for scattering and absorption). Laor & Netzer (1989) presented a first attempt in this direction and found that even such models could not fit the CEDs of a large fraction of their sample of AGNs if they included the soft X-ray data (Netzer 1991, and references therein).

As soft excesses seem quite common in QSOs (Masnou et al. 1992; Comastri et al. 1992) and since they are expected to arise in accretion disks viewed at high inclination angles, then many AGNs (possibly 50%) should be oriented towards us in a highly nonrandom way; this seems unlikely. If the optical/UV and soft X-ray emission are really one feature, then the strength of the UV bump and the soft excess should be correlated in a sample of QSOs. This is not the case as shown by Masnou et al. (1992; although their study is hampered by the nonsimultaneity of the observations).

We had hoped to address the connection between the UV and soft X-ray emission further by studying the variability in the UV and soft X-ray band. Obviously, if both arise in the inner region of an accretion disk then their emission should vary in a correlated manner. Unfortunately, we not study such a correlation as no significant short-term variability was found in either band. In summary, the standard accretion disk models cannot easily explain H1821+643's CED, and it is too early to rule out alternatives to the accretion disk model, such as optically thin free-free radiation as suggested by Barvainis & Antonucci (1989) and Barvainis (1990).

This free-free model predicts an optical slope of about -0.1, but the slope determined by the optical continuum in H1821+643 is quite different: 0.37. Also, the extrapolation of the optical data down to radio frequencies with a slope of -0.1 overestimates the observed data points significantly except for the 20 cm point. Furthermore, the free-free spectrum is expected to exhibit a cutoff at $h\nu \sim kT$. Just as in the accretion disk models, this could occur in the UV leading to a discrepancy at soft X-ray energies, or in the EUV-XUV band failing to fit the UV data. Although we cannot reject the free-free model, the mismatch between the predicted and observed spectral shape in the optical/UV/X-ray bump do not strengthen its case. It should also be noted that the variability data on the soft X-ray excess in many AGNs (H1821+643 not one of them) seem to exclude its origin in an optically thin medium (Elvis et al. 1991).

10. CONCLUSIONS

We have presented simultaneous multiwavelength observations of the bright QSO H1821+643. The main aim of this investigation was to study the connection between the optical/UV bump and the soft X-ray excess, as both emissions are generally attributed to an accretion disk but observational evidence for this assumption is still lacking. We set out to study this through investigating the correlation of the short-term variability in the optical/UV and soft X-ray band, and by testing the applicability of the accretion disk models to the simultaneous continuum energy distribution. The former was preempted by the absence of significant, short-term variability in either the UV or X-ray bands. There is, however, evidence for long-term variability on a time scale of months to years in the optical and UV bands (both in spectral slope and flux), where the amplitude of the variability increases with frequency. By fitting the continuum energy distribution with thin accretion disk models we found that bare disk models cannot easily account for the emission in both the UV (with a flat slope in a νf_ν diagram) *and* the steep excess in the soft X-ray band. Alternative models involving free-free radiation are not particularly promising either.

The superior spectral and spatial resolution of *ROSAT* allowed us to isolate the emission originating in the QSO from the nearby white dwarf K1−16. The intrinsic X-ray spectrum of H1821+643 showed a typical power-law slope above ~ 0.3 keV, as detected by *ROSAT* and *Ginga*. There is evidence for a steep soft excess, which was fit equally well with a power-law, blackbody, or bremsstrahlung model. We also reported on the first detection of H1821+643 in the radio band. This radio-quiet QSO was found to have a substantial radio flux at 20 cm and a typical steep spectral slope. The radio image was extended at 20 cm and could be resolved into two components at 6 cm. We also detected an elliptical galaxy at 6 cm and 20 cm which is in the same cluster as the QSO. High-resolution X-ray imaging of H1821+643 would be very interesting to see if a similar structure is present in the X-ray band. It could also determine the existence of an intracluster medium, if any, and its contribution to the X-ray emission. Finally, we detected a Lyman-α forest line in the co-added ultraviolet spectrum at $z = 0.225$, which we identify with a foreground galaxy discovered by Schneider et al. (1992).

We are grateful for the able assistance of Rob Olling and Pauline McMahon with the analysis of the VLA observations. We thank John Hibbard for obtaining the optical image at KPNO, and L. C. Ho for assistance with the reduction of the Palomar optical spectrum. We are also grateful to Susan Neff for providing the 6 cm map. This research was supported by NASA *ROSAT* grant NAG 5-1606 and NASA *IUE* grant NAG 5-1425 to the Columbia Astrophysics Laboratory and by NSF grant AST-8957063 to A.V.F. One of us (M. K.) received a Grant-in-Aid of Research from the Academy of Sciences, through Sigma Xi, the Scientific Research Society, and a Fulbright Grant through the Netherlands America Commission for Educational Exchange. This paper is contribution number 489 of the Columbia Astrophysics Laboratory.

REFERENCES

Bahcall, J. N., Jannuzi, B. T., Schneider, D. P., Hartig, G. F., Bohlin, R., & Junkkarinen, V. 1991, ApJ, 377, L5
Bahcall, J. N., Jannuzi, B. T., Schneider, D. P., Hartig, G. F., & Green, R. F. 1992, ApJ, 397, 68
Barvainis, R. 1987, ApJ, 350, 537
———. 1990, ApJ, 353, 419
Barvainis, R., & Antonucci, R. 1989, ApJS, 70, 257
Bechtold, J., Czerny, B., Elvis, M., Fabbiano, G., & Green, R. F. 1987, ApJ, 314, 699
Bergeron, J. 1988, in QSO Absorption Lines, ed. J. C. Blades, D. Turnshek, & C. A. Norman (Cambridge: Cambridge Univ. Press), 127
Bohlin, R. C., & Grillmair, C. J. 1988, ApJS, 66, 209
Bohlin, R. C., & Holm, A. V. 1980, NASA *IUE* Newsletter, 10, 37
Bohlin, R. C., Savage, B. D., & Drake, J. F. 1978, ApJ, 224, 132
Cassatella, A., Lloyd, C., & Riestra, R. G. 1988, NASA *IUE* Newsletter, 35, 225
Chini, R., Kreysa, E., & Biermann, P. L. 1989, A&A, 219, 87
Crenshaw, D. M., Bruegman, O. W., & Norman, D. J. 1990, PASP, 102, 463
Comastri, A., Setti, G., Zamorani, G., Elvis, M., Giommi, P., Wilkes, B. J., & McDowell, J. C. 1992, ApJ, 384, 62
Cunningham, C. T. 1975, ApJ, 202, 788
Cutri, R. M., Wisniewski, W. Z., Rieke, G. H., & Lebofsky, M. J. 1985, ApJ, 296, 423
Czerny, B., & Elvis, M. 1987, ApJ, 321, 305
Edelson, R. A., & Malkan, M. A. 1986, ApJ, 308, 59
Elvis, M., Giommi, P., Wilkes, B. J., & McDowell, J. C. 1991, ApJ, 378, 537
Elvis, M., Wilkes, B. J., & McDowell, J. C. 1989, in Extreme Ultraviolet Astronomy, ed. R. F. Malina & S. Bowyer (NY: Pergamon)
Finley, D. S., Basri, G., & Bowyer, S. 1990, ApJ, 359, 483
Grauer, A. D., Bond, H. E., Liebert, J., Fleming, T. A., & Green, R. F. 1987, ApJ, 323, 271
Heiles, C. 1975, A&AS, 20, 37
Hutchings, J. B., & Neff, S. G. 1991, AJ, 101, 2001 (HN)
Kellerman, K. I., Sramek, R., Schmidt, M., Shaffer, D. B., & Green, R. 1989, AJ, 98, 1195
Kolman, M., Halpern, J. P., Shrader, C. R., & Filippenko, A. V. 1991, ApJ, 373, 57 (KHSF)
Kii, T., et al. 1991, ApJ, 367, 455
Krolik, J. H., & Kallman, T. R. 1988, ApJ, 324, 714
Laor, A., & Netzer, H. 1989, MNRAS, 238, 897
Malkan, M. A., & Sargent, W. L. W. 1982, ApJ; 254, 22
Masnou, J. L., Wilkes, B. J., Elvis, M., McDowell, J. C., & Arnaud, K. A. 1992, A&A, 253, 35
Miller, J. S., & Stone, R. P. S. 1987, The CCD Cassegrain Spectrograph at the Shane Reflector (Lick Obs. Tech. Rep. 48)
Morris, S. L., Weymann, R. J., Savage, B. D., & Gilliland, R. L. 1991, ApJ, 377, L21
Morrison, R., & McCammon, D. 1983, ApJ, 256, 92
Neff, S. G., & Hutchings, J. B. 1992, AJ, 103, 1746
Netzer, H. 1991, in Structure and Emission Properties of Accretion Disks, ed. C. Bertout, S. Collin, J. P. Lasota, & J. Tran Thanh Van (Gif-sur-Yvette: Editions Frontières), 177
Neugebauer, G., Miley, G. K., Soifer, B. T., & Clegg, P. E. 1986, ApJ, 308, 815
Pravdo, S. H., & Marshall, F. E. 1984, ApJ, 281, 570
Salzer, J. J. 1992, AJ, 103, 385
Sanders, D. B., Phinney, E. S., Neugebauer, G., Soifer, B. T., & Matthews, K. 1989, ApJ, 347, 29
Schneider, D. P., Bahcall, J. N., Gunn, J. E., & Dressler, A. 1992, AJ, 103, 1047
Seaton, M. J. 1979, MNRAS, 187, 73P
Snyder, W. A., & Wood, K. S. 1984, in X-Ray and UV Emission from Active Galactic Nuclei, ed. W. Brinkman & J. Truemper (Garching: Max-Planck Inst.), 114
Stark, A. A., Gammie, C. F., Wilson, R. W., Bally, J., Linke, R. A., Heiles, C., & Hurwitz, M. 1992, ApJS, 79, 77
Sun, W.-H., & Malkan, M. A. 1989, ApJ, 346, 68
Teays, T. J., & Garhart, M. P. 1990, NASA *IUE* Newsletter, 41, 94
Turner, T. J., & Pounds, K. A. 1989, MNRAS, 240, 833
Warwick, R. S., Barstow, M. A., & Yaqoob, T. 1989, MNRAS, 238, 917
Wilkes, B. J., Masnou, J. L., Elvis, M., McDowell, J., & Arnaud, K. 1989, in Proc. 23d ESLAB Symp., ed. J. Hunt & B. Battrick (Noordwijk: ESA), 1081
Williams, O. R., et al. 1992, ApJ, 389, 157
Wills, B. J., Netzer, H., & Wills, D. 1985, ApJ, 288, 94
Wood, K. S., et al. 1984, ApJS, 56, 507